Multiscale Computational Modeling of the Cardiopulmonary Consequences of Postnatal Hyperoxia with Implications for Preterm Born Children

Salla M Kim[1,2], Filip Jezek[3], Pim JA Oomen[1,2,4], Gregory P Barton[5], Feng Gu[3], Daniel A Beard[3], Kara N Goss[5,6], Mitchel J Colebank[1,7,8]*, and Naomi C Chesler[1,2]*

1. Edwards Lifesciences Foundation Cardiovascular Innovation and Research Center, University of California Irvine, Irvine, California, USA
2. Department of Biomedical Engineering, University of California Irvine, Irvine, California, USA
3. Department of Molecular & Integrative Physiology, University of Michigan, Ann Arbor, Michigan, USA
4. Center for Complex Biological Systems, University of California Irvine, Irvine, California, USA
5. Department of Internal Medicine, University of Texas Southwestern Medical Center, Dallas, Texas, USA
6. Department of Pediatrics, University of Texas Southwestern Medical Center, Dallas, Texas, USA
7. Department of Mathematics, University of South Carolina, Columbia, South Carolina, USA
8. Department of Biomedical Engineering, University of South Carolina, Columbia, South Carolina, USA

* Corresponding Author Emails: nchesler@uci.edu; mjcolebank@sc.edu

16-digit ORCID IDs:

- Salla M Kim: 0000-0002-5863-612X
- Filip Jezek: 0000-0003-0629-7389
- Pim JA Oomen: 0000-0002-0069-4538
- Gregory P Barton: 0000-0001-7471-5488
- Feng Gu: 0009-0006-8207-678X
- Daniel A Beard: 0000-0003-0974-2353
- Kara N Goss: 0000-0003-2015-9169
- Mitchel J Colebank: 0000-0002-2294-9124
- Naomi C Chesler: 0000-0002-7612-5796

Acknowledgements

National Institutes of Health, National Heart Lung and Blood Institute R01 HL154624 (NCC, DAB)

National Institutes of Health, National Heart Lung and Blood Institute R01 HL173346 (DAB)

MJC was supported in part through TL1 TR001415 through the National Center for Research Resources and the National Center for Advancing Translational Sciences, National Institutes of Health (NIH).

Original animal studies used for modeling were supported by the University of Wisconsin Clinical and Translational Science Award program, through National Center for Advancing Translational Sciences Grant UL1-TR-000427 (primary investigator M. Drezner; 4KL2-TR-000428-10, awarded to KNG), as well as a Joel Belt Pediatric Pulmonary Hypertension Research and Mentoring Grant through the Pulmonary Hypertension Association (Barst Award; PI KNG).

Statements and Declarations

Competing Interests: No conflicts of interest to disclose.

Abstract

Moderate to extreme preterm birth (<32 weeks gestation) affects cardiopulmonary structure and function and is associated with increased risk of heart failure through adulthood. The rat hyperoxia (Hx) model (term born; postnatal Hx exposure) captures biventricular changes, including at the cell- and organ-scale, and pulmonary vascular remodeling seen in preterm humans. However, synthesizing these measures across scales and organ systems is challenging. We hypothesized that in-silico modeling of biventricular mitochondrial, myofiber, and organ-scale function plus circulatory function could capture key features of cardiopulmonary abnormalities due to preterm birth. Therefore, we calibrated a multiscale model to subject-specific biventricular pressure-volume data previously obtained from Hx rats alongside normoxic (Nx) controls to investigate the abnormalities in cardiopulmonary function at multiple scales in this animal model of human preterm birth. The calibrated model demonstrates excellent agreement with the data and captures the expected pulmonary vascular changes and right ventricular dilation seen in preterm born children. Our multiscale modeling approach captures cardiopulmonary abnormalities across spatial scales and provides an innovative approach to explore the consequences of preterm birth beyond preclinical experimental data alone. This is a foundational step in understanding the impact of preterm birth on cardiopulmonary disease in childhood as well as adulthood.

KEYWORDS: preterm birth, cardiovascular, right ventricle, multiscale modeling, subject specific modeling

1. Introduction

Preterm birth (less than 37 weeks gestation) affects 1 in 10 live births in the United States (Bensley et al., 2010; Ferré et al., 2016). Neonatal care has improved over the last several decades, leading to an increased number of moderately to extremely preterm (less than 32 weeks gestation) born babies surviving into adulthood, with the consequence that we are only now beginning to understand the short- and long-term cardiopulmonary effects. The combination of the preterm newborn's underdeveloped cardiopulmonary system and their frequent need for life-saving respiratory support such as oxygen supplementation places them at high risk for cardiopulmonary injury (Bavineni et al., 2019). The cardiopulmonary consequences of preterm birth continue past infancy (Perez et al., 2020); through adulthood, those born premature are at increased risk for systemic and pulmonary hypertension, with an up to 17-fold increased risk for heart failure, cardiometabolic diseases, and stroke (Carr et al., 2017).

Clinically, the effects of preterm birth on cardiopulmonary structure and function span multiple spatial scales. At the organ and tissue scales these effects include reduced biventricular chamber sizes and microvascular density, ventricular hypertrophy and fibrosis, and changes to contractile function (Barton et al., 2021; François et al., 2022; Sixtus et al., 2024). Additionally, preterm neonates are exposed to a relatively hyperoxic (Hx) environment, and since mitochondrial DNA is very susceptible to oxidative damage, they are at high risk for cardiopulmonary mitochondrial dysfunction (Ali et al., 2024; Bavineni et al., 2019; Mohammadi et al., 2022). Coupled with high right ventricular (RV) afterload caused by an under-developed pulmonary circulation, these multiscale changes contribute to impaired RV-pulmonary vascular coupling (Dartora et al., 2021; Greer et al., 2021; Mulchrone et al., 2020).

Animal models can provide valuable functional data at multiple scales. The lung developmental stage at term for rodents is comparable to moderately to extremely preterm humans, and exposing rat pups born at term to 10-14 days of postnatal Hx (~85%) has been shown to capture key cardiopulmonary features seen in human preterm birth and is among the most used rat models of preterm birth (Berger & Bhandari, 2014; DeFreitas et al., 2024; O'Reilly & Thébaud, 2014; Ravizzoni Dartora et al., 2022; Velten et al., 2010). At postnatal day 21 (P21), which corresponds to early childhood, rat pups born at term exposed to 14 days of postnatal Hx have been shown to suffer from pulmonary hypertension, RV dysfunction, depressed cardiac mitochondrial oxidative capacity, and RV-pulmonary vascular uncoupling (Kumari 2019). These findings correspond to clinical findings in preterm-born children and provide useful insight into the disease state (Arjaans et al., 2022; Jeong et al., 2024; Kumari et al., 2021; Mulchrone et al., 2020). However, disparate measurements across multiple organ systems and scales can be challenging to synthesize. Mechanistic computational modeling can provide insights into the underlying mechanisms of the observed cardiopulmonary dysfunction and simulate physiological outputs that are beyond the available data, encouraging the generation of new hypotheses and experimental designs. Furthermore, subject-specific modeling can provide insight into disease progression in a single individual and generate an enhanced set of biomarkers for contrasting control and disease groups or identifying new disease subgroups (Colunga et al., 2020; Gu et al., 2025; Jones et al., 2021; Kachabi et al., 2025). Combining

experimental data with multiscale modeling can extend our understanding of complex processes, but also reduce the need for numerous, costly experiments that may be infeasible.

In this study, we tested our hypothesis that in-silico, subject-specific modeling of biventricular mitochondrial, myofiber, and organ-scale function and circulatory function could capture key features of the cardiopulmonary abnormalities due to preterm birth. With multiscale data previously collected in the postnatal Hx rodent model of preterm birth (Kumari et al., 2019; Patel et al., 2017), we simulated cardiopulmonary function using a multiscale cardiac model (Marzban et al., 2020) that includes the biventricular "TriSeg" heart model (Lumens et al., 2009) with calcium-dependent active myofiber force, and a closed-loop lumped-parameter circulation model as presented in Kim et al. (2023). We developed a workflow for subject-specific, multiscale modeling and analysis of pediatric, Hx rodents, including subject-specific sensitivity analyses and calibration of influential parameters to biventricular pressure-volume data. Overall, we confirmed our hypothesis that the model can represent RV and pulmonary vascular adaptations that are consistent with experimental and clinical findings. Our research provides a framework that combines literature and available experimental data to identify key mechanisms of cardiopulmonary dysfunction across spatial scales due to postnatal hyperoxia in rats. The model codes are publicly available to facilitate further independent studies.

2. Methods

2.1 Animal Data

Data collected from 12 rats (5F, 7M) exposed to neonatal hyperoxia as a model of preterm birth and 7 control rats (2F, 5M; normoxia only) are used here (Kumari et al., 2019). As detailed in Kumari et al. (2019), timed Sprague-Dawley dams delivered naturally to term. Within 12 hours of birth, pups were randomly exposed to either normal room air (Nx; 21% oxygen) or oxygen rich air (Hx; 85% oxygen) for 14 days. The Hx conditions mimic the relatively hyperoxic environment experienced by humans born preterm as previously demonstrated (Berger & Bhandari, 2014; Velten et al., 2010). The dams were rotated between chambers during the exposure period to avoid maternal oxygen toxicity. At P21, hemodynamic data including left ventricular (LV) and RV pressures and volumes were measured using invasive catheterizations and analyzed on Notocord Systems software (Notocord Systems, Croissy Sur Seine, France). The catheterizations were conducted via serial ventricular punctures using a 27g needle that was previously clotted (to prevent leakage) for both ventricles: the LV then the RV. Due to positioning there was no appreciable blood loss, but as an assurance a small piece of blotting paper was used to apply pressure while removing the needle and inserting the catheter. Sequential heart beats (20-50) were selected and processed in MATLAB software. The average pressure and volume signals were used for analysis and model calibration as further described in **Section 2.5**. The data displayed in **Table 1** were used for nominal parameter estimations, the same data separated by sex are shown in **Table S1**, where other than RV end systolic volume (ESV), which was greater in the Hx females, there was no significant difference between the females and males

2.2 Data Processing

Because LV and RV pressure and volume readings were recorded sequentially rather than simultaneously, the measured cardiac cycle duration (T, in seconds) differed from the LV and RV due to heart rate variability. To correct this, we averaged the LV and RV cycle durations and used this single cycle duration for both ventricles. Differences between LV and RV stroke volume (SV, in µL) due to the asynchronous catheter recording were accounted for by setting a common SV for both ventricles based on the average LV stroke volume for each animal since the conductance catheter measurement is typically more accurate for the LV geometry (Wearing et al., 2025). There was less variability in the measured end-systolic volume (ESV) compared to the measured end-diastolic volume (EDV), so we used the measured RV ESV and let RV EDV = RV ESV + SV. Also, for several animal models, the recorded end-diastolic pressure was negative, a calibration error that was corrected by shifting the pressure curve upward to match the average end diastolic pressure of the remaining animals in the same condition (Nx, Hx) and sex (M, F) group. Finally, the catheter artifacts during isovolumetric contraction can occur due to catheter positioning (Wearing et al., 2025). Given that these artifacts are not physiological and do not correspond with the disease phenotype, we enforced isovolumetric contraction and relaxation in the data.

Table 1. Group Averages of Measured Data

Metric	Units	Nx (n = 7)	Hx (n = 12)	p
Female/Male	-	5(F)/7(M)	2(F)/5(M)	**-**
BW	g	**49.9** ± 1.2	**53.4** ± 2.8	***8.9e-3**
T	s	**0.190** ± 0.044	**0.179** ± 0.015	**NS**
SV	µL	**28** ± 9	**28** ± 7	**NS**
LV ESV	µL	**16** ± 9	**18** ± 8	**NS**
RV ESV	µL	**24** ± 11	**23** ± 9	**NS**
LV EDP	mmHg	**4.4** ± 2.0	**5.1** ± 1.4	**NS**
LV ESP	mmHg	**65** ± 9	**72** ± 11	**NS**
RV EDP	mmHg	**2.9** ± 1.5	**3.8** ± 1.5	**NS**
RV ESP	mmHg	**26** ± 3	**38** ± 6	***2.3e-4**

BW – body weight; T – time; SV – stroke volume; ESV – end systolic volume; EDV – end diastolic volume; EDP – end diastolic pressure; ESP – end diastolic pressure; LV – left ventricle; RV – right ventricle.
***** Indicates a significant difference from a two-sample unpaired student's t-test ($p<0.05$). NS **-** not significantly different.

2.3 Multiscale Model Overview

We present an adapted multiscale cardiovascular model that includes crossbridge- and calcium (Ca^{2+})-dependent myofiber mechanics embedded within the TriSeg model and a lumped parameter circulatory model as summarized in **Figure 1**. In total there are 54 parameters and 46 differential equations, including 33 for crossbridge mechanics, 3 for myofiber mechanics, 4 for

the TriSeg, and 6 for circulation dynamics. The model codes are available at https://github.com/sallakim/Multiscale-Hx-P21-Model-2025.

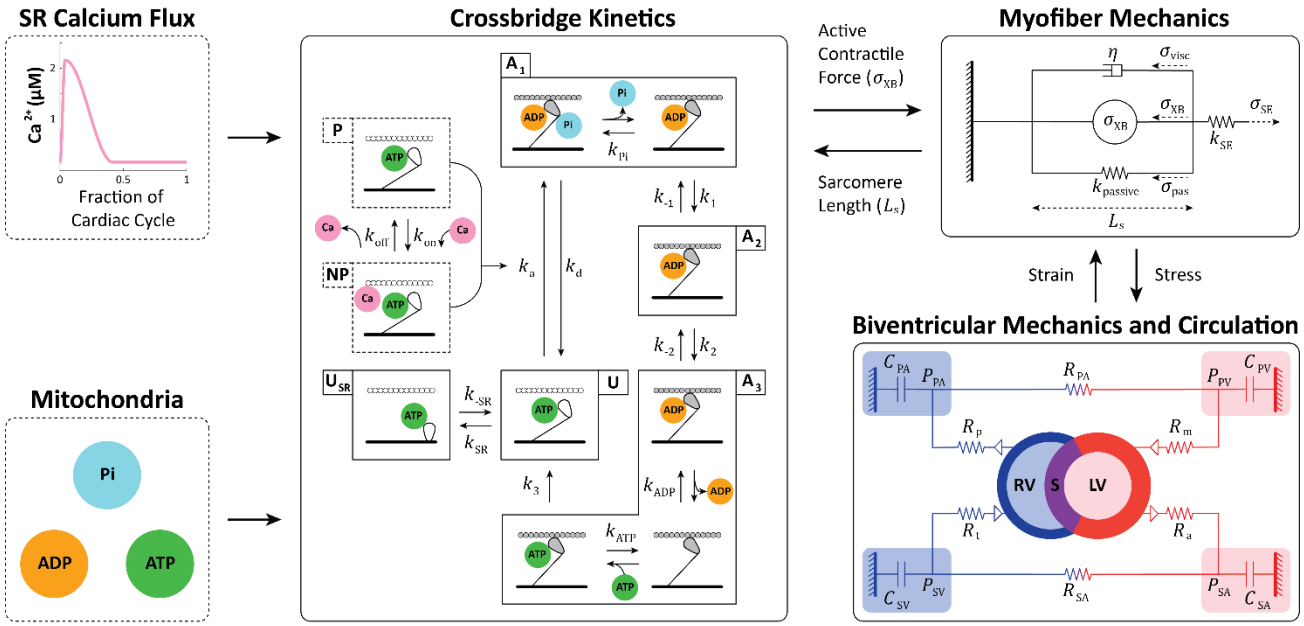

Figure 1. Multiscale, Multiorgan Cardiopulmonary Model Schematic

The model includes four sub-models: crossbridge kinetics, myofiber mechanics, biventricular mechanics, and circulation; with model inputs: sarcoplasmic reticulum (SR) calcium flux and mitochondria. The mitochondrial metabolites adenosine triphosphate (ATP), adenosine diphosphate (ADP), and inorganic phosphate (Pi) to determine rate constants in the crossbridge cycle, and a calcium (Ca) flux for Ca^{2+}-dependent activation and active stress generation. **Crossbridge Cycling.** The five-state crossbridge sub-model has three actin and myosin attached states and two unattached states. The three attached states are 1) loosely-attached, A_1, 2) strongly-attached, A_2, and 3) post-ratcheted and strongly-attached, A_3. The remaining states are 4) unattached, U, and 5) super-relaxed and unattached, U_{SR}. Together, these states describe crossbridge kinetics where $A_1 + A_2 + A_3 + U + U_{SR} = 1$. The binding and unbinding of ATP, ADP, and Pi to myosin and the transitions between states are dictated by rate constants, k. The unbinding rate of Pi within state A1 is k_{Pi}, the forward and reverse transition rate constants from state A1 to A2 are k_1 and k_{-1}. A3 state includes 3 "intermediate states" where ADP is released and ATP binds, and the rate of transitions for these intermediate states are k_{ADP} and k_{ATP}, correspondingly. The forward and reverse rate constants between the unbound, relaxed (U) and the super-relaxed (U_{SR}) states are given by k_{SR} and $k_{-\mathrm{SR}}$, respectively. The transition between permissible, P, and non-permissible, NP, pseudo-states is mediated by the binding, k_{on}, and unbinding, k_{off}, of Ca^{2+} to troponin C. This transition dictates the attachment rate, k_{a}, of myosin to actin, with a detachment rate, k_{a}. The crossbridge kinetics determine the active contractile force, σ_{XB}, used in the myofiber model. **Myofiber Mechanics.** The myofiber mechanics model is represented as a spring with active, σ_{XB}, a sarcomere length-dependent passive, σ_{pas}, viscous (η), σ_{visc}, and series elastic, σ_{SE}, force. **Biventricular Mechanics and Circulation**. The left and right ventricles (LV, RV) are represented as semi-spherical, separated by a septum (S), and comprised of thick walls according to the TriSeg model. The lumped-parameter circulation follows an electrical circuit analogy and includes the systemic arterial and venous compartments (SA, SV) and the pulmonary arterial and venous compartments (PA, PV) in addition to the LV and RV for a total of six compartments. The atrial (a), pulmonary (p), mitral (m), and tricuspid (t) valves are represented as diodes that only allow

forward flow with resistance, R. Vascular compartments are described as compliant chambers with compliance C.

2.3.1 Crossbridge Kinetics and Myofiber Mechanics Sub-Models

The myofiber mechanics sub-model integrates a Ca^{2+}-dependent crossbridge kinetics sub-model to simulate active and passive myocardial wall stress, which has been described in detail in Marzban et al. (2020). Here, we provide an overview of the model and only detail significant changes and model components particularly relevant to this study.

A moment-based distribution approach gives a system of five ordinary differential equations that represents three attached and two unattached crossbridge states (Graham, 2020; Tewari et al., 2016). The crossbridge mechanics model links the mechanical and biochemical kinetic processes by incorporating metabolite concentrations, adenosine triphosphate [ATP], adenosine diphosphate [ADP], and inorganic phosphate [Pi] into calculations of crossbridge transition rates.

The crossbridge model includes actin and myosin model components, and the states and transitions of the crossbridge kinetics sub-model are illustrated in **Figure 1**. The three actin and myosin attached states $A_{1\text{-}3}$ correspond to loosely attached, strongly attached, and post-ratcheted states, respectively. The remaining states are an unattached state, U, and an unattached, super-relaxed state, U_{SR}. The transitions between these states are dictated by the rate constants, k (s^{-1}). Together, these states and transition rates describe the crossbridge kinetics where $A_1 + A_2 + A_3 + U + U_{SR} = 1$. The transition from no Ca^{2+} bound, permissible, P, and Ca^{2+} bound, non-permissible, NP, is driven by Ca^{2+} binding, k_{on}, and unbinding, k_{off}, to troponin C. Finally, actin-myosin attachment is described by k_{a}, which is dependent on the Ca^{2+} dynamics.

The transition from non-permissible to permissible states is mediated by a Ca^{2+} activation function (Campbell et al., 2018). Here, we represent cytosolic Ca^{2+} concentrations as a function of time similar to other models (Chung et al., 2016; Hunter et al., 1998; Kim et al., 2023; Tran et al., 2017) with timing parameters that allow for subject-specific variability in contractile behavior, where

$$Ca^{2+}(t) = \begin{cases} Ca^{2+}_{\text{diastole}} + Ca^{2+}_{\text{amplitude}} \cdot 0.5\left(1 - \cos\left(\frac{\pi t}{T_{\text{S}}}\right)\right), & 0 \le t < T_{\text{S}} \\ Ca^{2+}_{\text{diastole}} + Ca^{2+}_{\text{amplitude}} \cdot 0.5\left(1 + \cos\left(\frac{\pi(t - T_{\text{S}})}{T_{\text{R}}}\right)\right), & T_{\text{S}} \le t \le T_{\text{S}} + T_{\text{R}} \\ Ca^{2+}_{\text{diastole}}, & \text{otherwise.} \end{cases} \quad (1)$$

$Ca^{2+}_{\text{diastole}}$ = 0.1610 μM is the minimum Ca^{2+} concentration at diastole and $Ca^{2+}_{\text{amplitude}}$ = 2 μM prescribes the amplitude of the sinusoidal relationship and therefore maximal Ca^{2+} concentration during systole. These values are set to correspond with the magnitudes in the data reported by (Marzban et al., 2020). The timing parameters include $T_{\text{S}} = k_{\text{TS}} \cdot T$ and $T_{\text{R}} = k_{\text{TR}} \cdot T$, where T (s) is the period of one cardiac cycle and k_{TS} and k_{TR} (unitless) are the

proportion of the cardiac cycle spent during increasing and decreasing Ca^{2+}, respectively. These cardiac timing parameters were calibrated for each animal according to the pressure and volume time course data (see **Section 2.6**).

Ca^{2+}-dependent active stress, $\sigma_{\mathrm{XB},i}$ (kPa) where $i = \mathrm{LV}, \mathrm{RV}, \mathrm{SEP}$, in the model is determined from the proportion of crossbridges in the attached, post-ratcheted state (A_3), defined by the 0th moment of state A_3, $P_{3,i}^0$ (unitless), and contributions from the attached bound, pre-ratcheted state (A_2), according to

$$\sigma_{\mathrm{XB},i}(t) = OV_{\mathrm{thick},i}(L_s) \cdot \left(k_{\mathrm{stiff},1}\left(P_{2,i}^1 + P_{3,i}^1\right) + k_{\mathrm{stiff},2} \cdot \Delta r \cdot P_{3,i}^0\right). \tag{2}$$

$P_{2,i}^1$ and $P_{3,i}^1$ (μm) are the 1st moment state of the A_2 and A_3 strain probability distributions, $k_{\mathrm{stiff},2}$ (kPa μm^{-1}) is the stiffness constant due to the working stroke of the crossbridge, $k_{\mathrm{stiff},1}$ (kPa μm^{-1}) is the stiffness constant due to the myosin-actin interaction, Δr (μm) is the crossbridge displacement associated with ratcheting deformation, and $OV_{\mathrm{thick},i}$ (unitless) is the fraction of thick filament overlap as a function of time-dependent sarcomere length, $L_{\mathrm{s},i}$ (μm). Additional details regarding crossbridge states can be found in Marzban et al. (2020) and Tewari et al. (2016).

We simplified the passive force, $\sigma_{\mathrm{pas},i}$ (kPa), formulation as in Kim et al. (2023) to be represented by a single exponential relation for collagen recruitment that depends on the time-dependent sarcomere length, $L_{\mathrm{s},i}$, and the contractile element length at zero active stress, L_{sc0} (μm). This is given by

$$\sigma_{\mathrm{pas},i}(t) = k_{\mathrm{passive}}(L_{\mathrm{s},i} - L_{\mathrm{sc0}})^{\gamma} \tag{3}$$

where k_{passive} (kPa μm^{-1}) is the passive stiffness constant, and γ (dimensionless) is the steepness of the length-tension relationship.

The full myofiber mechanics model includes contributions from the active force generated by the crossbridge kinetics, passive and viscous forces, and a series element force. The overall force balance in the model is

$$\sigma_{\mathrm{SE},i}(t) = \sigma_{\mathrm{XB},i}(t) + \sigma_{\mathrm{pas},i}(t) + \sigma_{\mathrm{visc},i}(t), \tag{4}$$

where $\sigma_{\mathrm{SE},i}$ (kPa) is the series elastic element and $\sigma_{\mathrm{visc},i}$ (kPa) is the viscous stress contributed from the dashpot (η) and determined by the rate of change of sarcomere length,

$$\sigma_{\mathrm{visc},i}(t) = \eta \frac{dL_{\mathrm{s},i}}{dt}. \tag{5}$$

2.3.2 Biventricular Mechanics and Circulation Sub-Models

For organ-scale dynamics, we model the heart and circulation as in Kim et al. (2023) using the biventricular TriSeg model (Lumens et al., 2009) and a zero-dimensional (0-D) lumped parameter circulatory model following an electrical circuit analogy with six compartments: LV, RV, systemic arteries (SA), systemic veins (SV), pulmonary arteries (PA), and pulmonary veins

(PV). The pericardium is typically removed or ruptured when PV loops are obtained experimentally in rodents as in the data used here. Thus, we remove the pericardial constraint, as in Kim et al. (2023), because it is an additional complexity that does not reflect the experimental data. Briefly, the ventricles are modeled as three semi-spherical thick-walls for the LV and RV free walls and septum (SEP). Active and passive cardiac myofiber mechanics and the TriSeg geometry determine the biventricular pressures which drive flow in the circulation. The SA, SV, PA, and PV systems are represented using Windkessel models with linear compliance, and flow between the compartments is dictated by Ohm's law with linear resistance. Finally, the mitral, aortic, tricuspid, and pulmonary valves are represented as pressure-sensitive resistances that only allow forward flow.

2.4 Nominal Model Parameterization for Pediatric, Hyperoxic Rats

The TriSeg and crossbridge models have been previously parameterized for adult humans, rats, and mice to study various cardiovascular disease cases (Colebank et al., 2023; Jones & Oomen, 2025; Kim et al., 2023; Lumens et al., 2009; Marzban et al., 2020; Pewowaruk et al., 2018; Tewari et al., 2016), but this is the first time these models have been parameterized for pediatric and hyperoxic rats. Crossbridge parameters from Marzban et al. (2020) were modified for early life Nx and Hx Sprague Dawley rats as described below.

2.4.1 Mitochondrial Inputs

Kumari et al. (2019) reported suppressed mitochondria complex 1 activity, increased mitochondrial density, and increased oxygen consumption in the RV myocardium of Hx animals at P21. Complex 1 is crucial for ATP production, as cytosolic ATP decreases with reduced complex 1 activity. In return, ADP and Pi accumulate due to the absence of ATP. To reflect these changes in the model, we assume a 5% decrease in ATP and a 5% increase in ADP and PI concentration in Hx animals.

2.4.2 Crossbridge Kinetics and Myofiber Mechanics Sub-Models Parameterization

Prakash et al. (1999) observed increased Ca^{2+} sensitivity of force with lower stiffness per area in the myocardium of Sprague Dawley neonates (P0-P3) compared to adults (P84) from skinned muscle experiments. Their findings suggest that this lower force in the neonatal myocardium is primarily from a 40% lower rate of crossbridge attachment; however, this effect may be exaggerated due to their two-state assumption. Additionally, the animals in our study are older, at P21 as compared to P0-P3. Therefore, we assume an intermediate reduction of 20% in the actin-myosin attachment rate constant, k_{a}, for P21 to reflect the older age.

Patel et al. (2017) found that passive stiffness of isolated RV trabeculae from Hx rats at P21 doubled in comparison to the Nx controls. Correspondingly, we increased the RV passive stiffness in the model, $\sigma_{\mathrm{pas,RV}}$, via the passive stiffness constant, $k_{\mathrm{passive,RV}}$, by a factor of two for the Hx animals.

Patel et al. (2017) also found an approximately 70% increase in the maximum Ca^{2+} activated force, F_{max}, at pCa = 4.5 (negative decadic logarithm of concentration, $[Ca^{2+}] = 10^{-4.5}$ = 32 μM) in the Hx animals compared to the Nx controls, indicating an increased Ca^{2+} sensitivity of

force. We conducted a model-based investigation to determine which crossbridge parameters increase pCa_{50} and $F_{\max}$. To do this, we first simulated the force-Ca^{2+} experiment using the isolated crossbridge and myofiber models. We fixed the sarcomere length at 2.2 µm, varied Ca^{2+} concentration from pCa 4.5 to pCa 7.0 and recorded the resulting force for several parameter changes. A total of 11 parameters can increase $F_{\max}$ or pCa_{50} to reproduce the experimentally observed changes to the force-Ca^{2+} (Patel et al., 2017) as summarized in **Table 2**. However, k_1, K_{D}, K_{T}, [ADP], and [ATP] must be changed by orders of magnitude outside of physiological domains to achieve the experimentally observed change in pCa_{50} and $F_{\max}$. Therefore, $k_{\mathrm{stiff},2}$, Δr, k_{on}, k_{off}, k_{a}, k_3, or some combination of these parameters are more likely to generate the observed changes in the myofiber contractile behavior. Further experimental data is required to determine which of these changes are responsible for the experimentally observed changes to the force-Ca^{2+} curve. In the absence of these data, we opted to decrease k_{off} and increase $k_{\mathrm{stiff},1}$ and $k_{\mathrm{stiff},2}$ to match the 1.04% leftward shift in pCa_{50} and 1.67% increase in $F_{\max}$ with Hx (Patel et al., 2017). The changes made to the Nx crossbridge parameters to represent Hx are summarized in **Table 3**.

Table 2. Parameters that Reproduce Experimentally Observed Changes the Force-Calcium Curve

Parameters	Experimental Observation (Patel et al., 2017)
$\uparrow k_{\mathrm{stiff},2}$, $\uparrow \Delta r$, or $\uparrow\uparrow k_1$	$\uparrow F_{\max}$
$\uparrow k_{\mathrm{on}}$, $\downarrow k_{\mathrm{off}}$, or $\uparrow k_{\mathrm{a}}$	$\uparrow pCa_{50}$
$\downarrow k_3$, $\downarrow\downarrow K_{\mathrm{D}}$, $\uparrow\uparrow K_{\mathrm{T}}$, $\downarrow\downarrow$ [ATP], or $\uparrow\uparrow$ [ADP]	$\uparrow F_{\max}$ and $\uparrow pCa_{50}$

Model parameters that when increased (↑) or decreased (↓) yield changes to the force-calcium curve that mimic experimental observations. The number of arrows dictates the relative magnitude of changes. $k_{\mathrm{stiff},2}$ - stiffness constant due to working stroke of the crossbridge; Δr - transition rate constant from loosely to strongly bound; k_{on} - binding rate of Ca^{2+} to Troponin C; k_{off} - unbinding rate of Ca^{2+} to Troponin C; k_{a} - myosin-actin rate of attachment; k_3 - myosin-actin detachment rate; K_{D} - ADP dissociation constant; K_{T} - ATP dissociation constant; [ATP] - ATP concentration; [ADP] - ADP concentration.

2.4.3 Biventricular Mechanics and Circulation Sub-Models Parameterization

Total blood volume is estimated by bodyweight (**Table 1**) using 0.06 mL/g of bodyweight as a reference for rodents (Lee & Blaufox, 1985). Nominal parameterizations for ventricular wall volumes and reference areas are calculated based on measured data from **Table 1**. First, to approximate the ventricular wall volumes, $V_{\mathrm{w},i}$ (cm^3), we used measured ventricular wall weights from a previous study and assumed a cardiac wall density of 1.055 g/mL (Gheorghe et al., 2019; Vinnakota & Bassingthwaighte, 2004). Individual LV and RV wall weights were not available from the rats with hemodynamic data available used here. A cohort of P21 Nx and Hx rats that did not undergo hemodynamic measurements (Kumari et al., 2019) had their wall weights, W_i, and bodyweight collected. Therefore, we calculated the average wall weight to bodyweight ratios, WR_i, from this cohort for the LV and septum, $WR_{\mathrm{LV+SEP}}$ (Nx, n =14, 3.8 ±

0.43; Hx, n = 12, 3.2 ± 0.37), where the LV is 2/3 and the SEP is 1/3 of this wall weight, and for the RV, WR_{RV} (Nx, n =14, 0.86 ± 0.13; Hx, n = 12, 1.00 ± 0.10). Then, given the wall weight to bodyweight ratio, we used bodyweight data to approximate the ventricular wall weights and subsequently the ventricular wall volumes for the subjects used in this present study. We approximated the midwall reference areas, $A_{\mathrm{m,ref},i}$, based on the measured LV and RV EDV data and an assumption of spherical geometry as detailed in Kim et al. (2023). Therefore, the nominal parameter calculations for the TriSeg geometry are consistent across all subjects and the nominal parameters vary due to variations in the animal data (**Table 1**). Nominal TriSeg geometry parameters are used as initial starts for calibration as detailed in **Section 2.6**.

Table 3. Hyperoxia-Induced Crossbridge Parameter Changes from Normoxia to Match Data from (Patel et al., 2017)

Symbol	Definition	Percent Change
[ATP]	Cytosolic concentration of ATP	-5%
[ADP]	Cytosolic concentration of ADP	+5%
[Pi]	Cytosolic concentration of Pi	-5%
$k_{\mathrm{passive,RV}}$	RV myofiber passive stiffness constant	+100%
$k_{\mathrm{off,RV}}$	RV rate constant of Ca detaching from Troponin C	-40%
$k_{\mathrm{stiff,1,RV}}$	RV stiffness constant due to myosin–actin interaction	+70%
$k_{\mathrm{stiff,2,RV}}$	RV stiffness constant due to working stroke of crossbridges	+70%

2.5 Sensitivity Analysis and Parameter Subset Selection

To determine which parameters to estimate given the available data, we conducted a sensitivity analysis to understand how variations in parameters affect the model output (Olsen et al., 2019). Key predictive outcomes of the model are LV and RV pressure and volume signals, and we are interested in identifying which parameters, relative to the available data, are most influential. Thus, we restricted our analysis to determining the influence of organ-scale and cardiac timing parameters on dynamic pressure and volume signals for both the LV and RV, which yields 18 parameters:

$$\boldsymbol{\theta}_{\mathrm{sens}} = \left\{ \begin{matrix} C_{\mathrm{SA}}, C_{\mathrm{SV}}, C_{\mathrm{PA}}, C_{\mathrm{PV}}, R_{\mathrm{SA}}, R_{\mathrm{PA}}, R_{\mathrm{m}}, R_{\mathrm{a}}, R_{\mathrm{t}}, R_{\mathrm{p}}, \\ A_{\mathrm{m,ref,RV}}, A_{\mathrm{m,ref,LV}}, A_{\mathrm{m,ref,SEP}}, V_{\mathrm{w,RV}}, V_{\mathrm{w,LV}}, V_{\mathrm{w,SEP}}, k_{\mathrm{TS}}, k_{\mathrm{TR}} \end{matrix} \right\}. \tag{6}$$

We performed a local, derivative-based sensitivity analysis to determine how perturbations, h, to the parameters, $\boldsymbol{\theta}_{\mathrm{sens}}$, influence the model output, $\boldsymbol{y}$. Here, we use the combined vector of LV and RV pressure and volume outputs as our $\boldsymbol{y}$. We approximate the derivative using a centered-difference approach

$$\boldsymbol{S}_{\boldsymbol{\theta}}^{y}(t, \boldsymbol{\theta}_{\mathrm{sens}}) = \frac{y(t, \boldsymbol{\theta}_{\mathbf{sens}} + h\boldsymbol{e}_{\boldsymbol{i}}) - y(t, \boldsymbol{\theta}_{\boldsymbol{sens}} - h\boldsymbol{e}_{\boldsymbol{i}})}{2h}. \tag{7}$$

where $\boldsymbol{e}_{\boldsymbol{i}}$ is a unit vector in the ith direction. Given the various magnitudes of the parameters, we conduct sensitivity analysis on a log-scale, with h = 0.01. Larger values of S_{θ}^{y} indicate greater

sensitivity of the model to that parameter. To cover the parameter space, we performed the local sensitivity analysis on each of the Nx and Hx animals and their nominal parameters, corresponding to different values of $\boldsymbol{\theta}_{\mathbf{sens}}$.

We normalized the sensitivities (i.e., $S_\theta^y(t,\theta)/\max\left(S_\theta^y(t,\theta)\right)$) for each animal such that they varied from 0 to 1 (**Figure 2**), and the parameters with a strong effect (normalized sensitivity > 0.1) on the combined pressure and volume output (see **Equation 7**) were considered for additional analyses (Colunga et al., 2023). We used the sensitivity vectors to construct an approximate Fisher information matrix, $\boldsymbol{F} = \boldsymbol{S}_{\boldsymbol{\theta}}^{\boldsymbol{y}\top}\boldsymbol{S}_{\boldsymbol{\theta}}^{\boldsymbol{y}}$, and ensured that for the selected parameter subset the condition number $\boldsymbol{F}$ is less than 1e8 (Colebank et al., 2024).

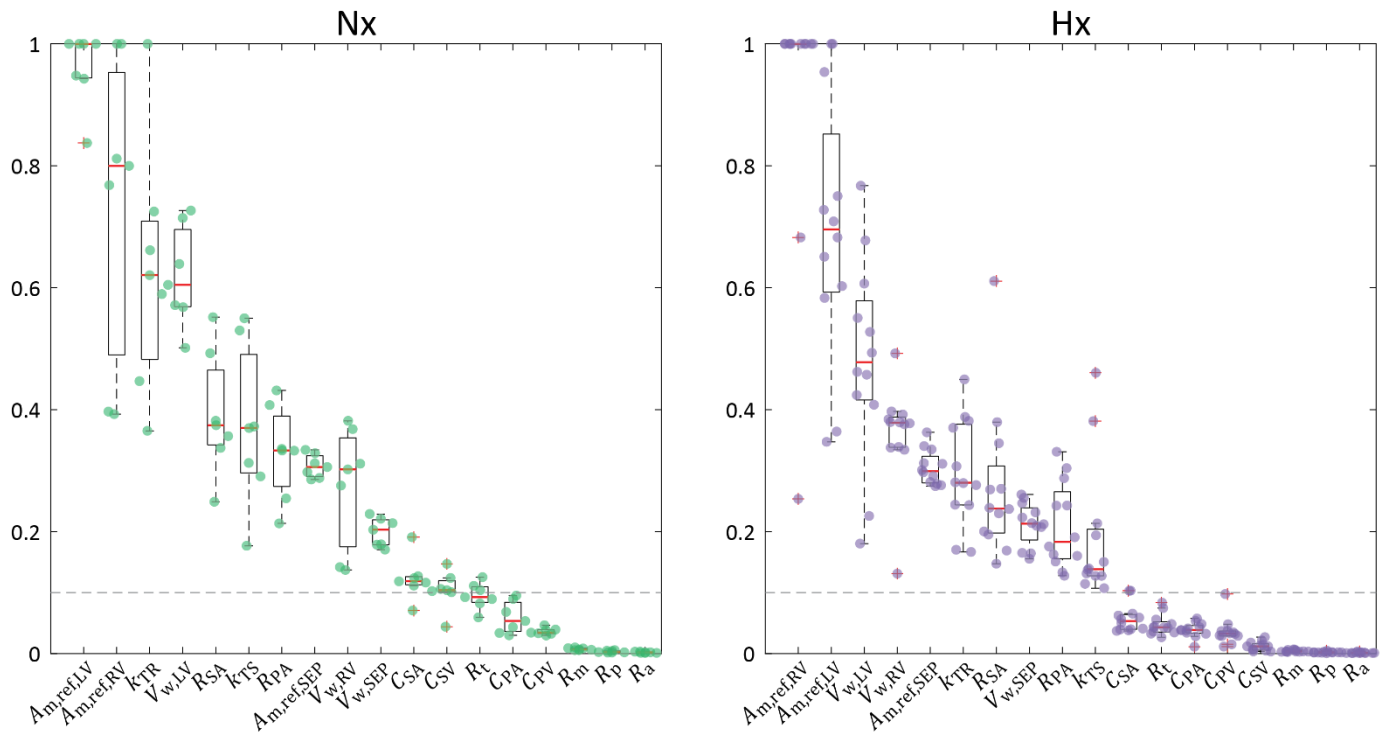

Figure 2. Sensitivity Analysis

Figure panels correspond to Nx (n = 7) and Hx (n = 12) experimental groups. The sensitivity of each parameter is normalized to each animal's maximum sensitivity i.e. parameter sensitivity varies from 0 to 1. For each animal, the corresponding normalized sensitivity is indicated by a point. The box-and-whisker plots provide the interquartile range of the normalized sensitivy for each parameter in each experimental group (mean shown in red). Parameters are ordered as most to least influential based on the mean sensitivity ranking across all animals in the same experimental group. A threshold of 0.1 is prescribed to delinate between influential and non-influential parameters. The top 10 parameters for both Nx and Hx are above the threshold and are the same. Two additional parameters, C_{SA} and C_{SV}, in Nx are also above the threshold.

2.6 Parameter Estimation and Model Calibration

From the sensitivity analysis, parameters with a normalized effect < 0.1 were fixed as non-influential. While all compliance parameters are below this threshold in Hx, C_{SA} and C_{SV} are

slightly above the 0.1 threshold in Nx. Other than C_{SA} and C_{SV}, all other parameters over the threshold were the same between Nx and Hx despite different orderings. We were interested in comparing parameter subsets between Nx and Hx and hence opted to use the same set of model parameters for each group and omitted C_{SA} and C_{SV} from the Nx group since they were only just over the threshold. Thus, our final parameter set for calibration for both Nx and Hx was

$$\boldsymbol{\theta}_{\mathrm{opt}} = \{R_{\mathrm{SA}}, R_{\mathrm{PA}}, A_{\mathrm{m,ref,LV}}, A_{\mathrm{m,ref,SEP}}, A_{\mathrm{m,ref,RV}}, V_{\mathrm{w,LV}}, V_{\mathrm{w,SEP}}, V_{\mathrm{w,RV}}, k_{\mathrm{TS}}, k_{\mathrm{TR}}\}. \tag{8}$$

To calibrate the model, we minimized the cost function, $J(\boldsymbol{\theta}_{\mathrm{opt}}) = \boldsymbol{r}(\boldsymbol{\theta}_{\mathrm{opt}})^{\top}\boldsymbol{r}(\boldsymbol{\theta}_{\mathrm{opt}})$, where $\boldsymbol{r}$ is the residual or difference between model simulations and measured data. We conducted our optimization on the log-scaled parameters to ensure similar magnitudes (Colunga et al., 2023). The components of $\boldsymbol{r}$ include time dependent and scalar differences in the model and data. The four dynamic residuals for the volume and pressure waveform data of both ventricles, $\boldsymbol{r}_{\mathrm{d}} = \{r_{\mathrm{V,LV}}, r_{\mathrm{V,RV}}, r_{\mathrm{P,LV}}, r_{\mathrm{P,RV}}\}$, are given by

$$\boldsymbol{r}_{\mathrm{d}} = \frac{1}{\sqrt{N}} \frac{\boldsymbol{y}^{\mathrm{d}}(t) - \boldsymbol{y}(t)}{\max(\boldsymbol{y}^{\mathrm{d}}(t))}, \tag{9}$$

where $\boldsymbol{y}(t) = \{\boldsymbol{V}_{\mathrm{LV}}(t), \boldsymbol{V}_{\mathrm{RV}}(t), \boldsymbol{P}_{\mathrm{LV}}(t), \boldsymbol{P}_{\mathrm{RV}}(t)\}$ represents the model outputs and $\boldsymbol{y}^{\mathrm{d}}(t)$ is the corresponding data. The model is resolved at timesteps that align with the waveform data, and the dynamic residuals are scaled based on the number of timesteps, $N = 50$, in the data. The eight static residuals for the end-diastolic and end-systolic pressure volume for both ventricles are defined as

$$\boldsymbol{r}_{\mathrm{s}} = \frac{\boldsymbol{Y}^{\mathrm{d}} - \boldsymbol{Y}}{\boldsymbol{Y}^{\mathrm{d}}}, \tag{10}$$

where the vector $\boldsymbol{Y} = \{EDV_{\mathrm{LV}}, EDV_{\mathrm{RV}}, ESV_{\mathrm{LV}}, ESV_{\mathrm{RV}}, EDP_{\mathrm{LV}}, EDP_{\mathrm{RV}}, ESP_{\mathrm{LV}}, ESP_{\mathrm{RV}}\}$ is the simulated pressure and volume, including end-diastolic and end-systolic volumes and pressures (EDV, ESV, EDP, and ESP), and $\boldsymbol{Y}^{\mathrm{d}}$ is the corresponding data. Therefore, the residual vector becomes $\boldsymbol{r} = \{\boldsymbol{r}_{\mathrm{d}}, \boldsymbol{r}_{\mathrm{s}}\}$. We used gradient-based, nonlinear least-squares global optimization with 20 randomized starting parameter vectors selected between ± 50% of the log-nominal values to minimize $J(\boldsymbol{\theta}_{\mathrm{opt}})$ (Colunga et al., 2023). We chose 20 initial starts to provide a robust optimal fit to the data. Of the 20 optimized parameter sets we chose the set with the smallest cost, J, to use for continued analyses. The upper and lower for the parameters are provided in **Table 4**. The overall simulation protocol is summarized in **Figure 3**.

Table 4. Parameter Bounds for Model Calibration

Parameters ($\boldsymbol{\theta}_{opt}$)	Upper and Lower Bounds

$A_{\mathrm{m,ref,RV}}, A_{\mathrm{m,ref,LV}}, A_{\mathrm{m,ref,SEP}}, V_{\mathrm{w,RV}}, V_{\mathrm{w,LV}}, V_{\mathrm{w,SEP}}$	$0.8 \cdot \log(\theta) < \log(\theta) < 1.2 \cdot \log(\theta)$
$R_{\mathrm{SA}}, R_{\mathrm{PA}}$	$0.1 \cdot \log(\theta) < \log(\theta) < 10 \cdot \log(\theta)$
k_{TS}	$0.001 < k_{TS} < 0.1$
k_{TR}	$0.3 < k_{TR} < 0.5$

$A_{\mathrm{m,ref,RV}}$, $A_{\mathrm{m,ref,LV}}$, $A_{\mathrm{m,ref,SEP}}$ - midwall reference area for the right ventricle (RV), left ventricle (LV), and septum (SEP), respectively; $V_{\mathrm{w,RV}}, V_{\mathrm{w,LV}}, V_{\mathrm{w,SEP}}$ - wall volume for the RV, LV, and SEP; R_{SA} - systemic arterial resistance; R_{PA} - pulmonary arterial resistance ; $k_{\mathrm{TS}}, k_{\mathrm{TR}}$ - proportion of cardiac cycle during systole and relaxation, respectively.

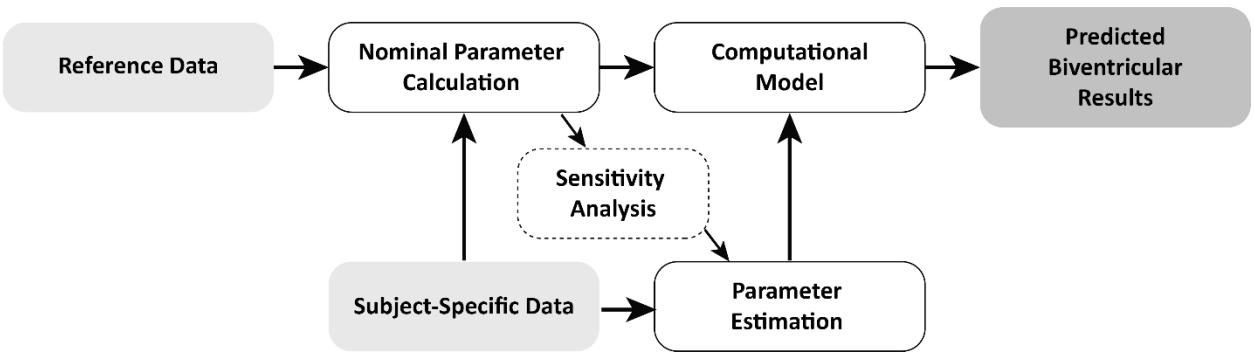

Figure 3. Simulation Protocol

2.7 Computed Metrics for Comparison and Statistical Methods

We compared computed ESV, EDV, ESP, and EDP to the measured data. In addition, we quantified myofiber power intensity and relative sarcomere shortening. To assess septal dynamics, we computed the TriSeg septal curvature (Kim et al., 2023; Lumens et al., 2009).

Model-predicted end-systolic and end-diastolic points are the minimum and maximum volumes and the maximum and minimum pressures at those volumes, respectively. Relative sarcomere shortening is computed as the change in sarcomere length throughout the cardiac cycle relative to the sarcomere length at the start of the cardiac cycle, $(\boldsymbol{L}_{\mathrm{s},i}(t) - \boldsymbol{L}_{\mathrm{s},i}(0))/\boldsymbol{L}_{\mathrm{s},i}(0)$.

We approximated myofiber power intensity (power per unit area) by first computing myofiber work intensity (work per unit area) throughout the cardiac cycle with discrete approximation of the integration of active myofiber force per unit area, $\sigma_{\mathrm{XB},i}$, with respect to sarcomere length, $\boldsymbol{L}_{\mathrm{s},i}$. Similarly, we approximated the derivative of the cumulative work intensity throughout the cycle with respect to time. We use the max absolute power intensity throughout the cardiac cycle as our comparison point across subjects.

We quantified septal "bounce" as the maximum drop in septal curvature during systole from the start of the cardiac cycle, $\Delta C_{\mathrm{m,SEP}}$ (cm^{-1}). The average curvature during systole, $\bar{C}_{\mathrm{m,SEP,systole}}$, was computed for comparison of septal flattening, or lack thereof, between Nx and Hx groups. Stroke work, SW, is calculated as the area of the pressure-volume loop.

We used a student's t-test to assess differences between 1) the computed model outputs and measured data, 2) the calibrated Nx and Hx parameters and model outputs and 3)

the calibrated parameters for the Hx male and female animals (**Figure S1**). Additionally, we assessed monotonic relationships in the parameters using Spearman's correlation coefficient (**Table 5**) and linear relationships between various modeling outputs using Pearson's correlation coefficient (**Table 7**) and visualized the data via scatter plots (**Figure 7**).

We performed a linear discriminant analysis (LDA) to assess separability of the two conditions using three sets of features (**Figure 8**). The first set uses rat data alone, namely volume and pressure data described in **Table 1**. The second set uses the calibrated parameter values as described in **Figure 5**. The third and final set integrated both the preclinical rat data and the model-derived features.

3. Results

3.1 Model Calibrations

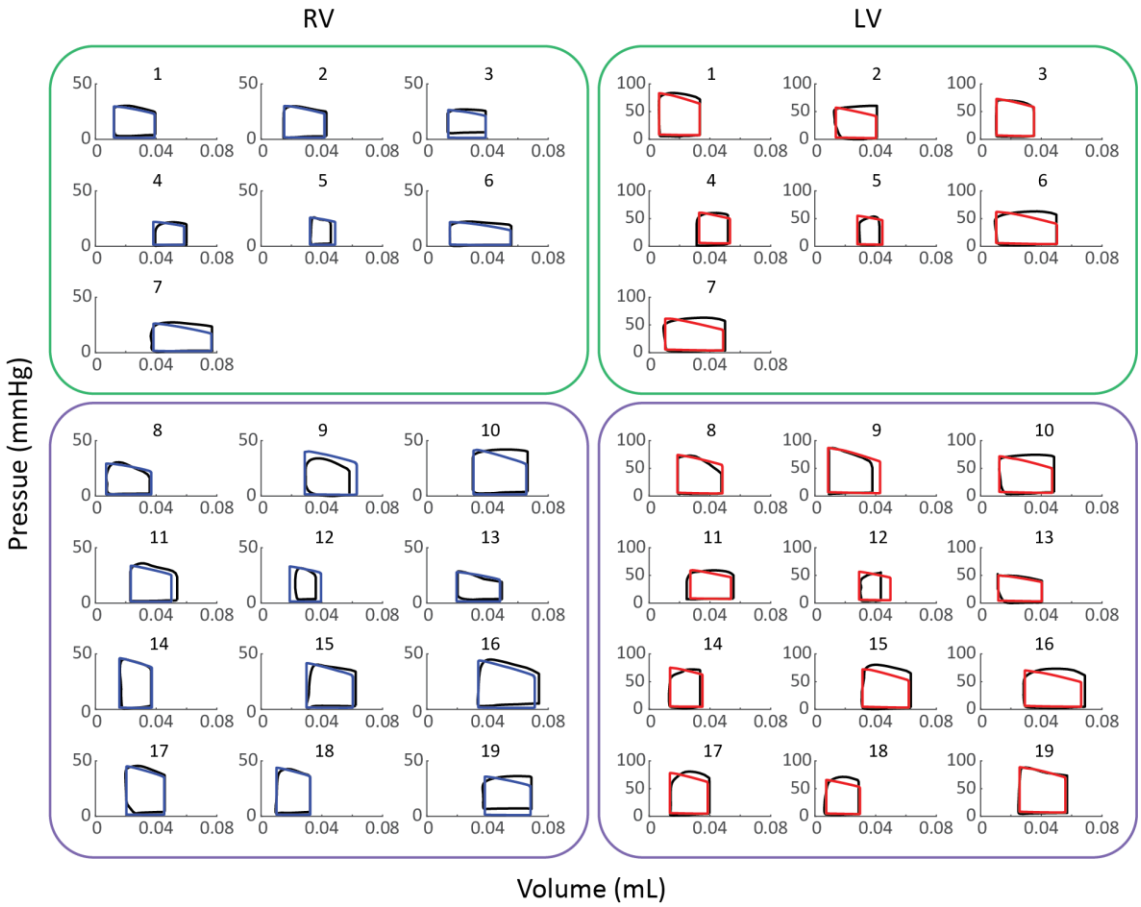

Figure 4. Calibrated Pressure Volume Loops

Calibrated Nx (green, subjects 1-7) and Hx (purple, subjects 8-19) subject-specific pressure volume loop simulations for the left ventricle (LV, red) and the right ventricle (RV, blue). The corresponding average of the data from 20+ cardiac cycles to which the model was calibrated is shown in black. The simulated pressure volume loops show good agreement with the measured data. The calibrated pressure and volume signals are shown in the Supplumenary Material.

The calibrated pressure-volume loop simulations demonstrated good agreement with the measured data as shown in **Figure 4**. In general, model simulations were within the bounds of variability seen in the 20 or more heartbeats of data. The model had difficulty matching RV EDP (**Table 5**), with an error between 2-4 mmHg.

Comparisons between the 10 model parameters ($\boldsymbol{\theta}_{\mathrm{opt}}$) calibrated to LV and RV pressure and volume data for Nx vs. Hx animals are shown in **Figure 5**. There are multiple significant differences in the calibrated parameters; the RV reference area, $A_{\mathrm{m,ref,RV}}$, and the systolic timing parameter, k_{TS}, are significantly increased in Hx, and the septal wall volume, $V_{\mathrm{w,SEP}}$, is significantly decreased in Hx compared to Nx. Although the difference is not significant, the pulmonary arterial resistance, R_{PA}, is notably increased in Hx (group mean for Hx: 24.3, for Nx: 16.7).

We compare the changes in calibrated parameters for each condition, separated by sex (**Table S14**). There is an insufficient number of female, Nx animals (Nx-F: n = 2) for statistical analysis, but R_{SA} and R_{PA} are notably increased in female Hx (66% and 135% increase in the means, respectively). Between the Nx and Hx males there are significant increases to $A_{\mathrm{m,ref,RV}}$ and k_{TS}, which aligns with sex-pooled results. Interestingly, there are no significant differences in $V_{\mathrm{w,SEP}}$ for the males (Nx-M: 0.0299, Hx-M: 0.0297); in this case the finding in the sex-pooled group can be attributed to the female subjects (Nx-F: 0.0973, Hx-F: 0.0173). When we consider sex differences in the parameters for each condition, we observe that R_{SA} and R_{PA} are significantly greater for the Nx males (116% and 140% increase in the means, respectively) than the females, with no significant differences between the Hx males and females. Additionally, R_{PA} and $V_{\mathrm{w,SEP}}$ were markedly greater for the Hx males (41% and 72% increase in the means, respectively) compared to the females.

The computational model takes on average 1-2 seconds on a laptop to provide simulation results. This time can increase to up to a minute of computation time if the parameterization leads to stiff dynamics in the systems, issues with solving with differential algebraic equations, or reaching steady state. Optimizing all 20 initial parameter estimates takes between one to four hours when run in parallel on a six-core machine. We use a trust-region-reflection algorithm in the lsqnonlin.m function from MATLAB with function evaluations limited to 2000 but otherwise use the default settings. The tolerance for parameter changes, function evaluation, and the step size is set to 1e-6. Finally, the objective function values are calculated using the residual functions in equations (9-10). The objective function values for the optimal solutions are on the order of 10^{-1}.

In effort to circumvent identifiability issues and local minima in our objective function, we combine our local sensitivity analysis with a multistart optimization as described in **Section 2.6**. The 20 optimized parameters cluster close to the optimal parameter set, but the parameters are numerically unique, and small differences in parameter values lead to differences in pressure and volume output signals. This outcome suggests that the model outputs are unique for each parameter combination and is consistent with Colebank and Chesler (2022), where a more in-depth identifiability analysis was done on a similar model using

the TriSeg infrastructure. We credit the identifiability of the model parameters in this study to the high-fidelity pressure-volume data.

Table 5. Comparison of Model Outputs to Corresponding Data

Metric	Units	Nx (n = 7)		R^2	Hx (n = 12)		R^2
		Data	Model		Data	Model	
LV EDV	μL	**44** ± 7	**44** ± 8	**0.99**	**47** ± 11	**46** ± 10	**0.98**
LV ESV	μL	**16** ± 9	**16** ± 10	**0.96**	**18** ± 8	**18** ± 9	**0.99**
RV EDV	μL	**52** ± 13	**51** ± 14	**0.99**	**52** ± 14	**51** ± 13	**0.97**
RV ESV	μL	**24** ± 11	**24** ± 12	**0.95**	**23** ± 9	**23** ± 10	**0.99**
LV EDP	mmHg	**4.4** ± 2.0	**4.6** ± 1.8	**0.98**	**5.1** ± 1.4	**4.9** ± 1.5	**0.97**
LV ESP	mmHg	**65** ± 9	**65** ± 10	**0.98**	**72** ± 11	**68** ± 11	**0.95**
RV EDP	mmHg	**2.9** ± 1.5	**1.4** ± 0.079	**0.56**	**3.8** ± 1.5	**1.4** ± 0.099	**0.14**
RV ESP	mmHg	**26** ± 3	**26** ± 3.2	**0.97**	**38** ± 6	**34** ± 8	**0.99**

R^2 - Spearman's correlation coefficient.

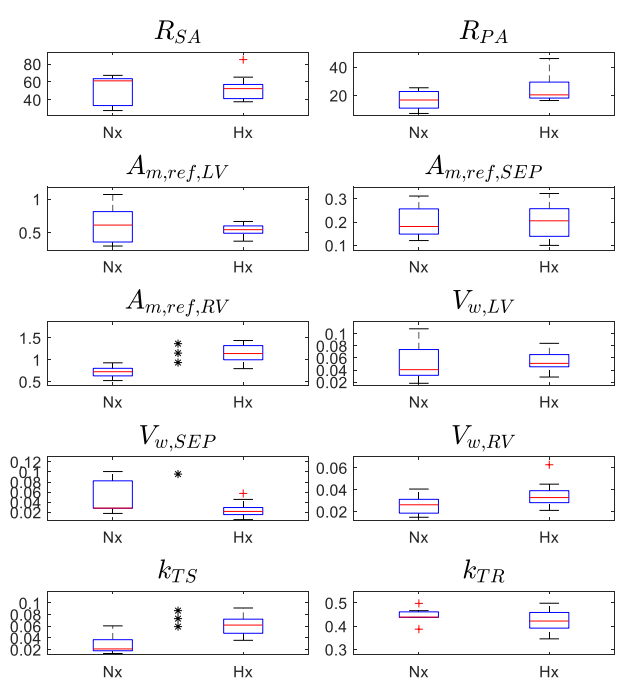

Figure 5. Calibrated Model Parameters (θ_{opt}) for Nx and Hx

Comparison of calibrated model parameter distributions for Nx and Hx, where $\boldsymbol{\theta}_{\mathrm{opt}} = \{R_{\mathrm{SA}}, R_{\mathrm{PA}}, A_{\mathrm{m,ref,LV}}, A_{\mathrm{m,ref,SEP}}, A_{\mathrm{m,ref,RV}}, V_{\mathrm{w,LV}}, V_{\mathrm{w,SEP}}, V_{\mathrm{w,RV}}, k_{\mathrm{TS}}, k_{\mathrm{TR}}\}$. * Indicates a significant difference from an unpaired two-sample student's t-test (p<0.05); ** (p<0.01); *** (p<0.001).

3.2 Model Predictions

As expected, mean pulmonary arterial pressure (mPAP) was elevated in Hx (**Table 6**). There was no difference in RV myofiber power intensity for the Hx group compared to the Nx group (**Table 6**) despite a prescribed increase in myofiber stiffness attributed to Hx (**Table 3**). However, the absolute RV myofiber length averaged over the cardiac cycle, $\bar{L}_{\mathrm{s,RV}}$, was lower in Hx than in Nx (**Table 6, Figure S2**), which suggests less engagement through the Frank-Starling Mechanism. The increased $A_{\mathrm{m,ref,RV}}$ in Hx (**Figure 5**) corresponds with the reduction in $\bar{L}_{\mathrm{s,RV}}$.

Model simulations revealed abnormal septal behavior during systole in Hx characterized by a rapid decrease (flattening towards the LV) and then subsequent rapid increase to baseline septal curvature near the start of ejection, or septal bounce (**Figure 6**). The septal drop, $\Delta C_{\mathrm{m,SEP}}$, in Hx was nearly 8 times larger than in Nx (**Table 6**). The mean curvature over systole, $\bar{C}_{\mathrm{m,SEP,systole}}$, was lower in Hx than Nx, although this difference was not significant (**Table 6**). The nature of the bounce includes an almost mirrored return to normal baseline septal curvature after the initial rapid curvature drop. Thus, there were minimal differences in $\bar{C}_{\mathrm{m,SEP,systole}}$ between Nx and Hx (**Table 6**).

We calculated the ratio of pulmonary arterial resistance to compliance as a metric of afterload and their product, the RC-time constant. The resistance-compliance ratio captures the effect of both altered resistance and compliance as contributors to afterload. Their ratio nearly doubled in Hx, which aligns with expected increases to right ventricular afterload. The RC-time constant is maintained across the conditions, consistent with clinical data in the pulmonary circulation (Tedford et al., 2012).

We performed a Pearson's Test for linear relationships between multiple model outputs and parameters (**Table 7**) and visualized these relationships in **Figure 7.** The clinical measure, mPAP, has a significant and moderate positive relationship with the model-predicted septal curvature drop, $\Delta C_{\mathrm{m,SEP}}$. In turn, the model-predicted $\Delta C_{\mathrm{m,SEP}}$ has a significant and moderate positive relationship with metrics associated with RV function, including RV SW and $A_{\mathrm{m,ref,RV}}$.

Visualization of the LDA results, **Figure 8**, demonstrate increased separability with the inclusion of model-derived features compared to rat data alone. The analysis applied to the data alone results in partial overlap between the Nx and Hx groups and therefore limited separability. However, the LDA performed on the calibrated model parameters (**Figure 5**) alone are clearly separated, and the separation increases when the rat data and model parameters are combined. This suggests that model-derived parameters, including those representing unmeasurable physiological biomarkers, can provide additional discriminatory information.

Table 6. Nx vs Hx Metrics

Symbol	Definition	Units	Nx (n = 7)	Hx (n = 12)	Change	p
mPAP	Mean pulmonary arterial pressure	mmHg	22.9 ± 3.2	33.7 ± 5.7	+47.2%	*2.5e-4
-	Myofiber Power Intensity	W m^2	5.07	5.49	+8.3%	NS
$\bar{L}_{\mathrm{s,RV}}$	Average RV sarcomere length	µm	2.04 ± 0.13	1.55 ± 0.02	-24%	*3.4e-10
$\Delta C_{\mathrm{m,SEP}}$	Septal curvature drop	cm^{-1}	0.19 ± 0.13	1.66 ± 0.45	+774%	*1.9e-7
$\bar{C}_{\mathrm{m,SEP,systole}}$	Average septal curvature in systole	cm^{-1}	2.59 ± 0.95	2.21 ± 0.61	-14.7%	NS
-	Pulmonary arterial compliance	cm^3 kPa^{-1}	0.027 ± 0.003	0.020 ± 0.003	- 25.4%	*5.5e-4
-	Ratio of pulmonary arterial resistance to compliance	cm^{-6} kPa^2 s	786 ± 331	1509 ± 630	+92%	*1.2e-2
RC-time constant	Product of pulmonary arterial resistance and compliance	s	0.563 ± 0.219	0.588 ± 0.190	4.6%	NS

* Indicates a significant difference from a student's t-test (p<0.05). NS - not significant.

Table 7. Pearson's Tests for Linear Relationships

Input 1	Input 2	ρ	p
$\Delta C_{\mathrm{m,SEP}}$	RV SW	0.51	*1.2e-3
$\Delta C_{\mathrm{m,SEP}}$	mPAP	0.60	*5.9e-5
$\Delta C_{\mathrm{m,SEP}}$	$A_{\mathrm{m,ref,RV}}$	0.48	*2.8e-2

Correlation (ρ) coefficient and significance (p) for linear relationships. *Indicates a significant linear relationship (p<0.05).

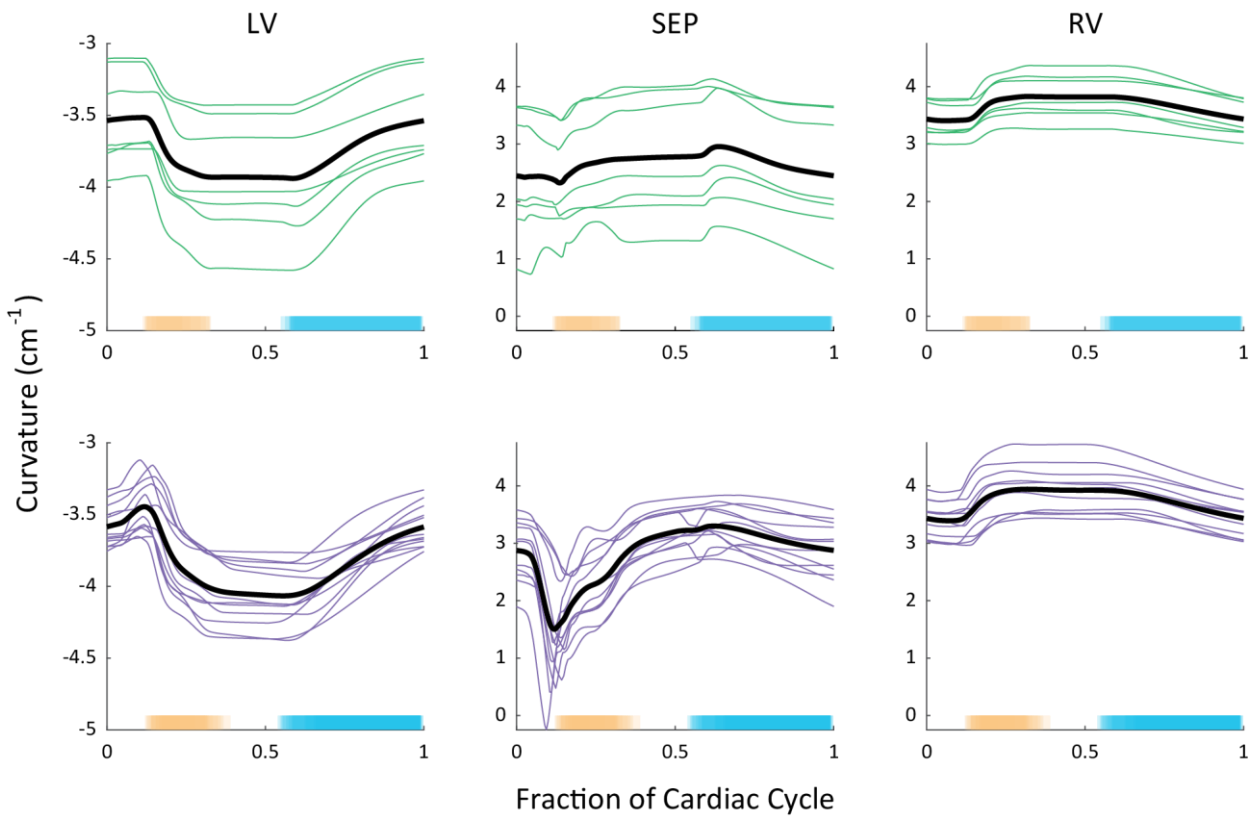

Figure 6. Curvature Predictions

Septal curvature from the start of the cardiac cycle for individual Nx and Hx animals. The x-axis is time-normalized to one cardiac cycle and the individual animal data is averaged (black) for ease of comparison. A lower septal curvature indicates flattening of the septum towards the LV. LV - left ventricle; RV - right ventricle.

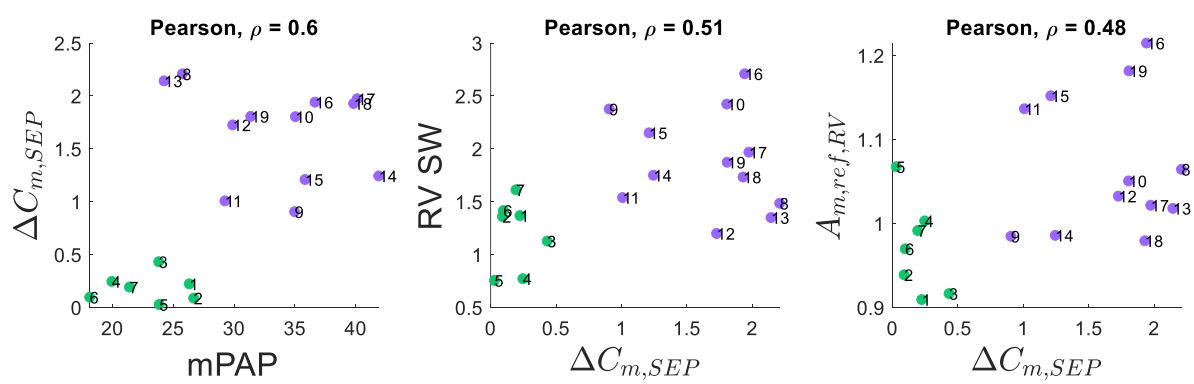

Figure 7. Relationships Between Model Outputs

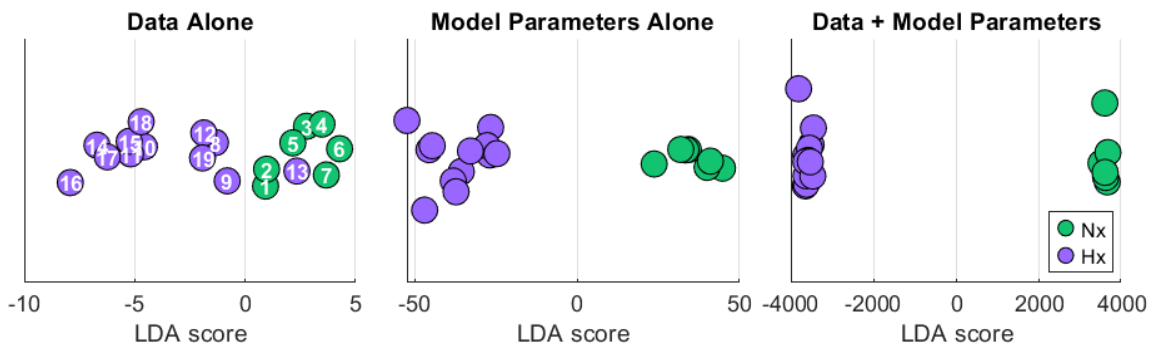

Figure 8. Linear Discriminant Analysis

LDA projections demonstrating separability of Nx and Hx conditions using rat data, calibrated model parameters, and combined data and model parameters. The combined feature set demonstrates the greatest amount of separability between the conditions.

4. Discussion

In this study, we developed subject-specific, multiscale models of the cardiopulmonary system in rodents that demonstrated an excellent fit to the experimental data and captured cardiopulmonary abnormalities that are consistent with the clinical literature on preterm born subjects. Our results highlight the multiscale nature of the cardiopulmonary consequences of postnatal Hx with implications for preterm born individuals and provide a framework for further exploration of cardiopulmonary disease manifestation into adulthood.

4.1 Simulation and Sensitivity Analysis

Versions of the multiscale cardiac model (Marzban et al., 2020) and TriSeg model (Kim et al., 2023) have demonstrated the ability to capture physiological hemodynamics in adult rats and humans, but the model has not been previously calibrated to pediatric and Hx cardiopulmonary data; therefore, we applied established approaches for model calibration that are scalable and promote identifiability. Colebank and Chesler (2022) demonstrated that in the context of biventricular, multiscale models for the study of pulmonary hypertension and RV function, right heart catheterization alone still yields identifiability issues and that at least some LV data is important to obtain. In this study, we had access to both RV and LV catheterization data; however with over 50 parameters in the full multiscale model and limited cellular-scale data, all parameters cannot be inferred simultaneously (Colebank et al., 2024).

To overcome this, we fixed parameters at the cellular-scale based on prior Nx rodent models (Marzban et al., 2020) and literature data in preterm birth and neonates (Patel et al., 2017; Prakash et al., 1999). We then used local sensitivity analysis to identify the most influential parameters for model calibration. Our findings in **Figure 2** show similar parameter effects in both Nx and Hx animals. However, the sensitivity of pressure-volume simulations to RV reference area increased in Hx, with nearly all Hx animals showing $A_{\mathrm{m,ref,RV}}$ as the most important parameter. Conversely, Hx sensitivity to LV reference area was smaller than Nx, again suggesting a shift in dominance between the two ventricles. Similar conclusions can be made

for the wall volumes, $V_{\mathrm{w,RV}}$ and $V_{\mathrm{w,LV}}$. These shape parameters have been identified as highly influential in other modeling studies (Colebank & Chesler, 2022; Jones & Oomen, 2025). In general, valve resistance and vascular compliance parameters were the least influential on pressure and volume outputs.

Our approach parallels methods employed by computational preterm studies combining physics-based mathematical modeling with subject data. For example, May et al. (2023) combined clinically measured cardiovascular anatomical and functional data from infants with a closed-loop computational model of the neonatal circulation. Subject data was partitioned for direct input into the model, parameter estimation, and verification of model predictions. For our study, more data is required for verification of model predictions as discussed in the limitations (**Section 4.7**).

4.2 Pressure-volume Loop Calibration

End-diastolic and end-systolic pressures and volumes have greater relevance than the intermediate points in the cardiac cycle, thus we put greater relative weight on the static end-systolic and end-diastolic measures in the calibration cost function. With this approach we were able to reach a global minimum across multiple randomized starting points, and the calibrated model simulations predict subject specific pressure-volume dynamics within the bounds of variability in data. A similar weighting approach was used by Colunga et al. (2023), which considered dynamic pressure data in the right heart and pulmonary artery along with static pressure data. The authors concluded similarly that static data corresponding to systolic and diastolic function were informative for parameter estimation, but that timeseries data provided additional insight. Our model consistently under-predicted RV EDP by 2-4 mmHg (**Table 5**). However, overall, the group averages of the calibrated model outputs were consistent with the corresponding group averages of the measured data. Note that we limited the number of model parameters to prioritize identifiability and interpretability of the parameters rather than include more non-identifiable parameters that provide a better fit at the expense of this interpretability. The ability of the model to match organ-level dynamics for individual subjects without detailed information on microscale mechanisms is a strength of our study.

Subject-specific modeling allowed us to compare the relationships between multiple model-predicted outputs and parameters, which can help determine relationships between multiple clinically relevant metrics (**Figure 7**, **Table 7**). Additionally, findings from our LDA analysis (**Figure 8**) suggest that incorporating mechanistic modeling can provide further insights into disease mechanisms that are not captured through preclinical measures alone. With more data, unsupervised machine learning may help stratify subjects into treatment cohorts based on non-invasive measures and model outputs (Gu et al., 2025; Jones et al., 2021), however the present dataset is too small for robustness in these analysis techniques. Given this limitation in experimental data, the mechanistic model could be used to generate synthetic data for training of these machine learning models as in Jones and Oomen (2025), although that is beyond the scope of this work.

4.3 Mechanisms of RV Hypercontractility

Our model investigations indicate multiple mechanisms by which myofiber contractile function may be altered from Nx to Hx. At least six parameters in the crossbridge model modulate Ca^{2+} sensitivity and maximum Ca^{2+} activated force within physiologically relevant ranges (**Table 2**). As detailed in our analysis in **Table 3**, the combination of decreasing the rate of Ca^{2+} unbinding from Troponin C via k_{off} and increasing $k_{\mathrm{stiff,1}}$ and $k_{\mathrm{stiff,2}}$ yields the expected changes in Ca^{2+} sensitivity and maximum Ca^{2+} activated force. Equivalent increases to Ca^{2+} binding to Troponin C rate k_{on} and decreases to k_{off} yield the same steady-state increase in Ca^{2+} sensitivity as assessed by the force-pCa curve (Chung et al., 2016; Dowrick et al., 2023; Kreutziger et al., 2011; Saad et al., 2023), which is also reflected in the model. However, there are distinct differences in the dynamic force development and relaxation of the myofiber when k_{on} versus k_{off} is altered (Chung et al., 2016). Namely, an increase in Ca^{2+} sensitivity due to decreased k_{off} yields slower relaxation kinetics than increased k_{on}. To confirm the mechanism of increased RV myofiber power with Hx and/or preterm birth, dynamic Ca^{2+} sensitivity experiments (Chung et al., 2016) could be used to measure k_{on} and k_{off}. Thus, our multiscale model provides a viable approach for testing multiple physiological hypotheses that may drive changes in the RV during postnatal Hx exposure. This innovative integration of data across multiple studies enables a robust testing of established hypotheses that is typically infeasible using experimental data alone.

RV myofiber power intensity is not significantly changed in Hx compared to Nx (**Table 6**) despite increased RV SW and directly imposed RV myofiber contractility changes (as in **Table 3**) to mimic experimental observation in Hx. However, there are numerous mechanisms that contribute to contractile function (Sharifi Kia et al., 2021), and this mismatch suggests additional mechanisms contributing to unchanged myofiber power intensity yet increased SW. For example, the time fraction for the rise of calcium development, k_{TS}, is significantly increased in Hx, which suggests an increased time for contraction contributes to overcoming the increased afterload in Hx. While RV myofibers are more contractile in Hx, the absolute RV sarcomere length was significantly reduced in Hx when compared to Nx, which corresponds to less engagement through the Frank-Starling mechanisms. Direct measurement of sarcomere length in whole organs is possible (Botcherby et al., 2013) but was not performed here to validate these predictions. Thus, direct translation of model sarcomere length to in vivo measures should be made with caution. In the model, sarcomere length is dependent on ventricular wall area and therefore represents the mechanical changes experienced by the ventricular wall. Together, these observations suggest a less efficient RV, which warrants further exploration.

4.4 Abnormal Septal Dynamics as a Marker of Altered RV Contractile Function and Pulmonary Hypertension

In our study, average septal curvature during systole ($\bar{C}_{\mathrm{m,SEP,systole}}$) did not significantly decrease in Hx despite significantly increased mPAP (**Table 6**). We attribute this result, at least in part, to the nature of septal bounce phenomenon wherein the curvature rapidly decreases, but then just as rapidly increases to return to baseline curvature. Clinically, assessment of septal flattening can be highly variable (Mourani et al., 2015), however septal flattening has been

observed in echocardiographic studies of nearly 300 preterm infants at P7 with pulmonary hypertension (Mourani et al., 2015) and over 200 infants at risk for pulmonary hypertension with systolic septal flattening as quantified by an LV end-systolic eccentricity index above 1.3 (Abraham & Weismann, 2016).

While average septal curvature over systole ($\bar{C}_{\mathrm{m,SEP,systole}}$) was a poor metric for differentiation between Hx and Nx in our simulations, our results showed significant correlations between septal bounce during systole and RV dilation as well as septal bounce during systole and RV SW (**Table 7**), which corresponds with observed correlations between flattening and RV dilation (Mourani et al., 2015) and flattening and RV systolic dysfunction (Abraham & Weismann, 2016). A previous study found that rapid leftward septal motion (equivalent to $\Delta C_{\mathrm{m,SEP}}$) during early LV diastole is a marker of worsening RV function in chronic pulmonary arterial hypertension resulting from interventricular relaxation desynchrony and altered RV contraction (Palau-Caballero et al., 2017). While our subject population is distinct from that of Palau-Caballero et al., their findings demonstrate the utility of septal bounce as a metric for altered contractile function. Therefore, we suggest that systolic septal bounce may be a more sensitive noninvasive marker of altered RV contractile function and acute pulmonary arterial hypertension than absolute flattening in pediatric subjects. That said, the complexities in the multiscale model make it difficult to isolate the exact reason for changes in curvature and warrant further investigation. Future experiments that report cardiac wall shortening and dynamics prior to ex-vivo tissue analysis may reveal the multiscale links between RV function, septal motion, and cellular or subcellular processes.

4.5 Sex Differences

In the preclinical dataset, the female Hx rats had increased RV ESV compared to the males (mean of 29 µL vs 19 µL), which was reflected in the model, but otherwise there were no significant differences between the males and females in the data or in calibrated model parameters (**Table S1, S14**). That said, pulmonary arterial resistance, R_{pa}, (Hx-F: 19.6, Hx-M: 27.6) is dramatically higher in the males. Interestingly, the greater pulmonary arterial resistance in males occurs despite comparable RV ESP (Hx-F: 36, Hx-M: 39). We also note a smaller stroke volume in males versus females, which may explain part of this difference given that $R \propto \Delta P/SV$. This greater resistance suggests a worse cardiopulmonary status and corresponds with clinical findings that preterm neonates are more often male, and males exhibit worse outcomes and greater death rates than females (Goss et al., 2020; Ingemarsson, 2003).

In the rat Hx model of preterm birth, sex differences at 1 year have been identified (Cantu et al., 2023); at P21, the age considered in this study, the observed sex differences thus far are limited (Kumari et al., 2019; Rahmani et al., 2024). Therefore, further mechanisms of sex differences may be identified by modeling rat Hx data at 1 year (P365) or by including sex hormones in a growth and remodeling framework (Lakshmikanthan et al., 2025).

4.6 Implications for Human Preterm Birth Modeling

Modeling and simulation of the cardiovascular system is a crucial component of precision medicine, especially with the development of medical digital twins (Colebank et al.,

2024). The primary goals of cardiovascular systems modeling are two-fold: 1) to augment clinical and experimental data for knowledge generation, as in this study, and 2) to be a clinical tool for diagnosis and treatment. It should be noted that modeling approaches typically focus on calibration and validation to adult patients, whereas this approach is relatively limited in its application in pediatrics. When developing tools for clinical use a key consideration is the data availability (Niederer, Lumens, et al., 2019).

In this study, dynamic pressure and volume data were available for model calibration, but in a clinical setting the available data is likely to be far more limited (e.g., systolic and diastolic metrics via echocardiography) and require a modification of our approach. The timepoint of the rats in this study corresponds to human early childhood, from whom it is particularly challenging to collect data. Versions of the mechanistic model have been parameterized for both adult humans, mice, and rats, and now, young rats; therefore, it is reasonable to expect that the model can be applied to infant humans in the future. Depending on the age of the subject, data collected in those born preterm can include systemic blood pressure, heart rate, oxygen saturation, major vessel diameters (via MRI), blood velocity profiles (via ultrasound), and cardiac geometry and morphology/tissue properties (such as fibrosis, via cardiac MR) (Barton et al., 2021; Philip A. Corrado et al., 2021; P. A. Corrado et al., 2021; François et al., 2022; Kumari et al., 2021; May et al., 2023). In young adults and adults, right heart catheterization may be justified (Goss et al., 2018), but in infants this invasive method is typically only used in cases of suspected severe pulmonary hypertension, congenital heart defects or when surgery is already required. Taking these factors into consideration, it is reasonable to consider that a typical clinical dataset would include cardiac volumes and geometry (area, thickness), static systemic blood pressure estimates (subsequently LV pressure), static cardiac pressure estimates, total blood volume estimates, and estimated time spent across cardiac stages. However, the more limited dataset may not be sufficient for robust model calibration (Colebank & Chesler, 2022), in which case the addition of statistical models may be useful or necessary to derive meaningful insights (Gu et al., 2025; Peirlinck et al., 2021). Echocardiography is often the first noninvasive step to determine disease severity and the possible need for catheterization (Mourani et al., 2008), thus one application of modeling could be to reduce the uncertainty in echocardiography-based predictions (Mourani et al., 2015) and aid in the identification of high-risk patients who would benefit from early intervention.

At a microscale level, major components of contractile function are maintained across species; however, humans express primarily beta-myosin heavy chain (MHC) isoforms with small amounts of alpha-MHC in the ventricles while the reverse is true in rats (Prodanovic et al., 2022). Therefore, implications derived from analyses of contractile function in early life Hx rats for preterm humans must be considered with caution (Niederer, Campbell, et al., 2019; Reiser et al., 2001). A key difference between the two MHC isoforms is in the transition rates between various crossbridge states. The 5-state crossbridge model presented in this study includes rate transitions that can be tuned to data, and future work could include adjusting crossbridge kinetics (Johnson et al., 2019; Prodanovic et al., 2022) to account for differences in alpha and beta isoforms, allowing for improved translation of experimental rodent data to human subjects (Niederer, Campbell, et al., 2019).

4.7 Limitations

The major limitations of this study include limited mitochondrial and crossbridge-scale data, lack of imaging data, and a small subject population. As a result, validation of many model parameters, especially at the cell and tissue level, must await additional data. Collection of subject-specific crossbridge data would allow for model calibration at the cellular-scale and greater insights into cellular mechanisms of increased myofiber power with Hx. This data would also narrow the possibilities of Hx crossbridge dynamics, as outlined in **Table 3**. Understanding the connection between energetics and mechanics is also important for parameterizing and calibrating the model and requires further study and data collection. Additionally, wall weights or volumes for each animal were not available and we used an approximation based on group averages. Access to subject-specific wall geometry data would improve our ability to further personalize the model. We did not have access to imaging data, such as echo or MRI, to confirm the abnormal septal motion in Hx that the model predicts. However, our findings correspond with clinical studies in preterm infants and infants with pulmonary hypertension and computational studies of pulmonary hypertension, providing support for our observations. Though our study includes pressure-volume data from both ventricles, we find that the end-diastolic pressure-volume relationship is relatively flat, hence our model results to do not show nonlinear EDPVR dynamics. Indeed, the data also exhibits a flat EDPVR, thus the model and data are aligned in this regard. Finally, the small subject population prevented dividing the dataset into calibration and validation cohorts, which is considered a best practice (Colebank et al., 2024) and limited our ability to interrogate sex differences (n=2 females in the Nx group).

5. Conclusions

By calibrating a multiscale cardiac mechanics and closed loop circulation model to data from an established rodent model of preterm birth, we highlight key cardiovascular consequences of postnatal Hx exposure during early life. We provide a framework that can take complex, multiscale and multiorgan models, and parameterize them such that disease mechanisms can be tested, and intrinsically subject-specific parameters are calibrated to available data. Moreover, our study is the first to consider a subject-specific, multiscale cardiopulmonary model for analyzing the effects of postnatal Hx in rodents. Our investigations generate testable hypotheses regarding mechanisms of a hypercontractile RV due to postnatal Hx and lay the foundation for future studies on the cardiopulmonary consequences of preterm birth in humans.

6. Supplementary Material

With this manuscript all model codes are provided, available at https://github.com/sallakim/Multiscale-Hx-P21-Model-2025.

7. References

Abraham, S., & Weismann, C. G. (2016). Left Ventricular End-Systolic Eccentricity Index for Assessment of Pulmonary Hypertension in Infants. *Echocardiography*, *33*(6), 910-915. https://doi.org/https://doi.org/10.1111/echo.13171

Ali, M. A., Gioscia-Ryan, R., Yang, D., Sutton, N. R., & Tyrrell, D. J. (2024). Cardiovascular aging: spotlight on mitochondria. *American Journal of Physiology-Heart and Circulatory Physiology*, *326*(2), H317-H333. https://doi.org/10.1152/ajpheart.00632.2023

Arjaans, S., Fries, M. W. F., Schoots, M. H., Schilte, C. F. M., Roofthooft, M. T. R., Vrijlandt, E. J. L. E., Bos, A. F., Kooi, E. M. W., & Berger, R. M. F. (2022). Clinical Significance of Early Pulmonary Hypertension in Preterm Infants. *The Journal of Pediatrics*, *251*, 74-81.e73. https://doi.org/10.1016/j.jpeds.2022.07.039

Barton, G. P., Corrado, P. A., Francois, C. J., Chesler, N. C., Eldridge, M. W., Wieben, O., & Goss, K. N. (2021). Exaggerated Cardiac Contractile Response to Hypoxia in Adults Born Preterm. *J Clin Med*, *10*(6). https://doi.org/10.3390/jcm10061166

Bavineni, M., Wassenaar, T. M., Agnihotri, K., Ussery, D. W., Lüscher, T. F., & Mehta, J. L. (2019). Mechanisms linking preterm birth to onset of cardiovascular disease later in adulthood. *Eur Heart J*, *40*(14), 1107-1112. https://doi.org/10.1093/eurheartj/ehz025

Bensley, J. G., Stacy, V. K., De Matteo, R., Harding, R., & Black, M. J. (2010). Cardiac remodelling as a result of pre-term birth: implications for future cardiovascular disease. *European Heart Journal*, *31*(16), 2058-2066. https://doi.org/10.1093/eurheartj/ehq104

Berger, J., & Bhandari, V. (2014). Animal models of bronchopulmonary dysplasia. The term mouse models. *American Journal of Physiology-Lung Cellular and Molecular Physiology*, *307*(12), L936-L947. https://doi.org/10.1152/ajplung.00159.2014

Botcherby, E. J., Corbett, A., Burton, R. A. B., Smith, C. W., Bollensdorff, C., Booth, M. J., Kohl, P., Wilson, T., & Bub, G. (2013). Fast Measurement of Sarcomere Length and Cell Orientation in Langendorff-Perfused Hearts Using Remote Focusing Microscopy. *Circulation Research*, *113*(7), 863-870. https://doi.org/doi:10.1161/CIRCRESAHA.113.301704

Campbell, K. S., Janssen, P. M. L., & Campbell, S. G. (2018). Force-Dependent Recruitment from the Myosin Off State Contributes to Length-Dependent Activation. *Biophys J*, *115*(3), 543-553. https://doi.org/10.1016/j.bpj.2018.07.006

Cantu, A., Gutierrez, M. C., Dong, X., Leek, C., Anguera, M., & Lingappan, K. (2023). Modulation of recovery from neonatal hyperoxic lung injury by sex as a biological variable. *Redox Biol*, *68*, 102933. https://doi.org/10.1016/j.redox.2023.102933

Carr, H., Cnattingius, S., Granath, F., Ludvigsson, J. F., & Edstedt Bonamy, A.-K. (2017). Preterm Birth and Risk of Heart Failure Up to Early Adulthood. *Journal of the American College of Cardiology*, *69*(21), 2634-2642. https://doi.org/https://doi.org/10.1016/j.jacc.2017.03.572

Chung, J. H., Biesiadecki, B. J., Ziolo, M. T., Davis, J. P., & Janssen, P. M. (2016). Myofilament Calcium Sensitivity: Role in Regulation of In vivo Cardiac Contraction and Relaxation. *Front Physiol*, *7*, 562. https://doi.org/10.3389/fphys.2016.00562

Colebank, M. J., & Chesler, N. C. (2022). An in-silico analysis of experimental designs to study ventricular function: A focus on the right ventricle. *PLOS Computational Biology*, *18*(9), e1010017. https://doi.org/10.1371/journal.pcbi.1010017

Colebank, M. J., Oomen, P. A., Witzenburg, C. M., Grosberg, A., Beard, D. A., Husmeier, D., Olufsen, M. S., & Chesler, N. C. (2024). Guidelines for mechanistic modeling and analysis in cardiovascular research. *Am J Physiol Heart Circ Physiol*, *327*(2), H473-h503. https://doi.org/10.1152/ajpheart.00766.2023

Colebank, M. J., Taylor, R., Hacker, T. A., & Chesler, N. C. (2023). Biventricular Interaction During Acute Left Ventricular Ischemia in Mice: A Combined In-Vivo and In-Silico Approach. *Annals of Biomedical Engineering*, *51*(11), 2528-2543. https://doi.org/10.1007/s10439-023-03293-z

Colunga, A. L., Colebank, M. J., & Olufsen, M. S. (2023). Parameter inference in a computational model of haemodynamics in pulmonary hypertension. *Journal of The Royal Society Interface*, *20*(200), 20220735. https://doi.org/doi:10.1098/rsif.2022.0735

Colunga, A. L., Kim, K. G., Woodall, N. P., Dardas, T. F., Gennari, J. H., Olufsen, M. S., & Carlson, B. E. (2020). Deep phenotyping of cardiac function in heart transplant patients using cardiovascular system models. *The Journal of Physiology*, *598*(15), 3203-3222. https://doi.org/https://doi.org/10.1113/JP279393

Corrado, P. A., Barton, G. P., Macdonald, J. A., François, C. J., Eldridge, M. W., Goss, K. N., & Wieben, O. (2021). Altered Right Ventricular Filling at Four-dimensional Flow MRI in Young Adults Born Prematurely. *Radiology: Cardiothoracic Imaging*, *3*(3), e200618. https://doi.org/10.1148/ryct.2021200618

Corrado, P. A., Barton, G. P., Razalan-Krause, F. C., François, C. J., Chesler, N. C., Wieben, O., Eldridge, M., McMillan, A. B., & Goss, K. N. (2021). Dynamic FDG PET Imaging to Probe for Cardiac Metabolic Remodeling in Adults Born Premature. *J Clin Med*, *10*(6). https://doi.org/10.3390/jcm10061301

Dartora, D. R., Flahault, A., Luu, T. M., Cloutier, A., Simoneau, J., White, M., Lapointe, A., Villeneuve, A., Bigras, J.-L., Altit, G., & Nuyt, A. M. (2021). Association of Bronchopulmonary Dysplasia and Right Ventricular Systolic Function in Young Adults Born Preterm. *Chest*, *160*(1), 287-296. https://doi.org/https://doi.org/10.1016/j.chest.2021.01.079

DeFreitas, M. J., Shelton, E. L., Schmidt, A. F., Ballengee, S., Tian, R., Chen, P., Sharma, M., Levine, A., Katz, E. D., Rojas, C., Abitbol, C. L., Hunter, J., Kulandavelu, S., Wu, S., Young, K. C., & Benny, M. (2024). Neonatal hyperoxia exposure leads to developmental programming of cardiovascular and renal disease in adult rats. *Sci Rep*, *14*(1), 16742. https://doi.org/10.1038/s41598-024-65844-1

Dowrick, J. M., Taberner, A. J., Han, J.-C., & Tran, K. (2023). Methods for assessing cardiac myofilament calcium sensitivity [Review]. *Frontiers in Physiology*, *14*. https://doi.org/10.3389/fphys.2023.1323768

Ferré, C., Callaghan, W., Olson, C., Sharma, A., & Barfield, W. (2016). Effects of Maternal Age and Age-Specific Preterm Birth Rates on Overall Preterm Birth Rates - United States, 2007 and 2014. *MMWR Morb Mortal Wkly Rep*, *65*(43), 1181-1184. https://doi.org/10.15585/mmwr.mm6543a1

François, C. J., Barton, G. P., Corrado, P. A., Broman, A. T., Chesler, N. C., Eldridge, M. W., Wieben, O., & Goss, K. N. (2022). Diffuse Myocardial Fibrosis at Cardiac MRI in Young Adults Born Prematurely: A Cross-sectional Cohort Study. *Radiol Cardiothorac Imaging*, *4*(3), e210224. https://doi.org/10.1148/ryct.210224

Gheorghe, A. G., Fuchs, A., Jacobsen, C., Kofoed, K. F., Møgelvang, R., Lynnerup, N., & Banner, J. (2019). Cardiac left ventricular myocardial tissue density, evaluated by computed tomography and autopsy. *BMC Med Imaging*, *19*(1), 29. https://doi.org/10.1186/s12880-019-0326-4

Goss, K. N., Beshish, A. G., Barton, G. P., Haraldsdottir, K., Levin, T. S., Tetri, L. H., Battiola, T. J., Mulchrone, A. M., Pegelow, D. F., Palta, M., Lamers, L. J., Watson, A. M., Chesler, N. C., & Eldridge, M. W. (2018). Early Pulmonary Vascular Disease in Young Adults Born Preterm. *Am J Respir Crit Care Med*, *198*(12), 1549-1558. https://doi.org/10.1164/rccm.201710-2016OC

Goss, K. N., Haraldsdottir, K., Beshish, A. G., Barton, G. P., Watson, A. M., Palta, M., Chesler, N. C., Francois, C. J., Wieben, O., & Eldridge, M. W. (2020). Association Between Preterm Birth and Arrested Cardiac Growth in Adolescents and Young Adults. *JAMA Cardiology*, *5*(8), 910-919. https://doi.org/10.1001/jamacardio.2020.1511

Graham, M. D. (2020). Generalized distribution-moment approximation for kinetic theories of muscular contraction. *Mathematical Biosciences*, *329*, 108455. https://doi.org/https://doi.org/10.1016/j.mbs.2020.108455

Greer, C., Harris, S. L., Troughton, R., Adamson, P. D., Horwood, J., Frampton, C., & Darlow, B. A. (2021). Right Ventricular Structure and Function in Young Adults Born Preterm at Very Low Birth Weight. *J Clin Med*, *10*(21). https://doi.org/10.3390/jcm10214864

Gu, F., Meyer, A. J., Ježek, F., Zhang, S., Catalan, T., Miller, A., Schenk, N. A., Sturgess, V. E., Uceda, D., Li, R., Wittrup, E., Hua, X., Carlson, B. E., Tang, Y.-D., Raza, F., Najarian, K., Hummel, S. L., & Beard, D. A. (2025). Identification of digital twins to guide interpretable AI for diagnosis and prognosis in heart failure. *npj Digital Medicine*, *8*(1), 110. https://doi.org/10.1038/s41746-025-01501-9

Hunter, P. J., McCulloch, A. D., & ter Keurs, H. E. D. J. (1998). Modelling the mechanical properties of cardiac muscle. *Progress in Biophysics and Molecular Biology*, *69*(2), 289-331. https://doi.org/https://doi.org/10.1016/S0079-6107(98)00013-3

Ingemarsson, I. (2003). Gender aspects of preterm birth. *BJOG: An International Journal of Obstetrics and Gynaecology*, *110*, 34-38. https://doi.org/https://doi.org/10.1016/S1470-0328(03)00022-3

Jeong, J., Lee, Y., Han, J., Kang, E., Kim, D., Kim, K.-s., Kim, E. A.-R., Lee, B. S., & Jung, E. (2024). Mitochondrial DNA mutations in extremely preterm infants with bronchopulmonary dysplasia. *Gene*, *910*, 148337. https://doi.org/https://doi.org/10.1016/j.gene.2024.148337

Johnson, C. A., Walklate, J., Svicevic, M., Mijailovich, S. M., Vera, C., Karabina, A., Leinwand, L. A., & Geeves, M. A. (2019). The ATPase cycle of human muscle myosin II isoforms: Adaptation of a single mechanochemical cycle for different physiological roles. *Journal of Biological Chemistry*, *294*(39), 14267-14278. https://doi.org/https://doi.org/10.1074/jbc.RA119.009825

Jones, C. E., & Oomen, P. J. A. (2025). Synergistic biophysics and machine learning modeling to rapidly predict cardiac growth probability. *Comput Biol Med*, *184*, 109323. https://doi.org/10.1016/j.compbiomed.2024.109323

Jones, E., Randall, E. B., Hummel, S. L., Cameron, D. M., Beard, D. A., & Carlson, B. E. (2021). Phenotyping heart failure using model-based analysis and physiology-informed machine learning. *J Physiol*, *599*(22), 4991-5013. https://doi.org/10.1113/jp281845

Kachabi, A., Altieri Correa, S., Chesler, N. C., & Colebank, M. J. (2025). Bayesian parameter inference and uncertainty quantification for a computational pulmonary hemodynamics model using Gaussian processes. *Comput Biol Med*, *194*, 110552. https://doi.org/10.1016/j.compbiomed.2025.110552

Kim, S. M., Randall, E. B., Jezek, F., Beard, D. A., & Chesler, N. C. (2023). Computational modeling of ventricular-ventricular interactions suggest a role in clinical conditions involving heart failure [Original Research]. *Frontiers in Physiology*, *14*. https://doi.org/10.3389/fphys.2023.1231688

Kreutziger, K. L., Piroddi, N., McMichael, J. T., Tesi, C., Poggesi, C., & Regnier, M. (2011). Calcium binding kinetics of troponin C strongly modulate cooperative activation and tension kinetics in cardiac muscle. *J Mol Cell Cardiol*, *50*(1), 165-174. https://doi.org/10.1016/j.yjmcc.2010.10.025

Kumari, S., Barton, G. P., & Goss, K. N. (2021). Increased mitochondrial oxygen consumption in adult survivors of preterm birth. *Pediatric Research*, *90*(6), 1147-1152. https://doi.org/10.1038/s41390-021-01387-9

Kumari, S., Braun, R. K., Tetri, L. H., Barton, G. P., Hacker, T. A., & Goss, K. N. (2019). Bimodal right ventricular dysfunction after postnatal hyperoxia exposure: implications for the preterm heart. *Am J Physiol Heart Circ Physiol*, *317*(6), H1272-h1281. https://doi.org/10.1152/ajpheart.00383.2019

Lakshmikanthan, A., Kay, M., & Oomen, P. J. A. (2025). Modeling the Interplay of Sex Hormones in Cardiac Hypertrophic Signaling. *bioRxiv*, 2025.2002.2024.639810. https://doi.org/10.1101/2025.02.24.639810

Lee, H. B., & Blaufox, M. D. (1985). Blood Volume in the Rat. *Journal of Nuclear Medicine*, *26*(1), 72-76. https://jnm.snmjournals.org/content/jnumed/26/1/72.full.pdf

Lumens, J., Delhaas, T., Kirn, B., & Arts, T. (2009). Three-wall segment (TriSeg) model describing mechanics and hemodynamics of ventricular interaction. *Ann Biomed Eng*, *37*(11), 2234-2255. https://doi.org/10.1007/s10439-009-9774-2

Marzban, B., Lopez, R., & Beard, D. A. (2020). Computational Modeling of Coupled Energetics and Mechanics in the Rat Ventricular Myocardium. *Physiome*. https://doi.org/0.36903/physiome.12964970

May, R. W., Talou, G. D. M., Argus, F., Gentles, T. L., Bloomfield, F. H., & Safaei, S. (2023). *An Image-Based Computational Model of the Newborn Cardiovascular System with Term and Preterm Applications* Functional Imaging and Modeling of the Heart: 12th International Conference, FIMH 2023, Lyon, France, June 19–22, 2023, Proceedings, Lyon, France. https://doi.org/10.1007/978-3-031-35302-4_49

Mohammadi, A., Higazy, R., & Gauda, E. B. (2022). PGC-1α activity and mitochondrial dysfunction in preterm infants. *Front Physiol*, *13*, 997619. https://doi.org/10.3389/fphys.2022.997619

Mourani, P. M., Sontag, M. K., Younoszai, A., Ivy, D. D., & Abman, S. H. (2008). Clinical Utility of Echocardiography for the Diagnosis and Management of Pulmonary Vascular Disease in Young Children With Chronic Lung Disease. *Pediatrics*, *121*(2), 317-325. https://doi.org/10.1542/peds.2007-1583

Mourani, P. M., Sontag, M. K., Younoszai, A., Miller, J. I., Kinsella, J. P., Baker, C. D., Poindexter, B. B., Ingram, D. A., & Abman, S. H. (2015). Early Pulmonary Vascular Disease in Preterm Infants at Risk for Bronchopulmonary Dysplasia. *American Journal of Respiratory and Critical Care Medicine*, *191*(1), 87-95. https://doi.org/10.1164/rccm.201409-1594OC

Mulchrone, A., Bellofiore, A., Douwes, J. M., Duong, N., Beshish, A. G., Barton, G. P., Francois, C. J., Eldridge, M. W., Goss, K. N., & Chesler, N. C. (2020). Impaired Right Ventricular-Vascular Coupling in Young Adults Born Preterm. *Am J Respir Crit Care Med*, *201*(5), 615-618. https://doi.org/10.1164/rccm.201904-0767LE

Niederer, S. A., Campbell, K. S., & Campbell, S. G. (2019). A short history of the development of mathematical models of cardiac mechanics. *Journal of Molecular and Cellular Cardiology*, *127*, 11-19. https://doi.org/https://doi.org/10.1016/j.yjmcc.2018.11.015

Niederer, S. A., Lumens, J., & Trayanova, N. A. (2019). Computational models in cardiology. *Nature Reviews Cardiology*, *16*(2), 100-111. https://doi.org/10.1038/s41569-018-0104-y

O'Reilly, M., & Thébaud, B. (2014). Animal models of bronchopulmonary dysplasia. The term rat models. *Am J Physiol Lung Cell Mol Physiol*, *307*(12), L948-958. https://doi.org/10.1152/ajplung.00160.2014

Olsen, C. H., Ottesen, J. T., Smith, R. C., & Olufsen, M. S. (2019). Parameter subset selection techniques for problems in mathematical biology. *Biol Cybern*, *113*(1-2), 121-138. https://doi.org/10.1007/s00422-018-0784-8

Palau-Caballero, G., Walmsley, J., Empel, V. V., Lumens, J., & Delhaas, T. (2017). Why septal motion is a marker of right ventricular failure in pulmonary arterial hypertension: mechanistic analysis using a computer model. *American Journal of Physiology-Heart and Circulatory Physiology*, *312*(4), H691-H700. https://doi.org/10.1152/ajpheart.00596.2016

Patel, J. R., Barton, G. P., Braun, R. K., Goss, K. N., Haraldsdottir, K., Hopp, A., Diffee, G., Hacker, T. A., Moss, R. L., & Eldridge, M. W. (2017). Altered Right Ventricular Mechanical Properties Are Afterload Dependent in a Rodent Model of Bronchopulmonary Dysplasia. *Front Physiol*, *8*, 840. https://doi.org/10.3389/fphys.2017.00840

Peirlinck, M., Costabal, F. S., Yao, J., Guccione, J. M., Tripathy, S., Wang, Y., Ozturk, D., Segars, P., Morrison, T. M., Levine, S., & Kuhl, E. (2021). Precision medicine in human heart modeling. *Biomechanics and Modeling in Mechanobiology*, *20*(3), 803-831. https://doi.org/10.1007/s10237-021-01421-z

Perez, A., Thiede, L., Lüdecke, D., Ebenebe, C. U., von dem Knesebeck, O., & Singer, D. (2020). Lost in Transition: Health Care Experiences of Adults Born Very Preterm—A Qualitative Approach [Original Research]. *Frontiers in Public Health*, *8*. https://doi.org/10.3389/fpubh.2020.605149

Pewowaruk, R. J., Philip, J. L., Tewari, S. G., Chen, C. S., Nyaeme, M. S., Wang, Z., Tabima, D. M., Baker, A. J., Beard, D. A., & Chesler, N. C. (2018). Multiscale Computational Analysis of Right Ventricular Mechanoenergetics. *J Biomech Eng*, *140*(8), 0810011-08100115. https://doi.org/10.1115/1.4040044

Prakash, Y. S., Cody, M. J., Housmans, P. R., Hannon, J. D., & Sieck, G. C. (1999). Comparison of cross-bridge cycling kinetics in neonatal vs. adult rat ventricular muscle. *Journal of Muscle Research & Cell Motility*, *20*(7), 717-723. https://doi.org/10.1023/A:1005585807179

Prodanovic, M., Geeves, M. A., Poggesi, C., Regnier, M., & Mijailovich, S. M. (2022). Effect of Myosin Isoforms on Cardiac Muscle Twitch of Mice, Rats and Humans. *Int J Mol Sci*, *23*(3). https://doi.org/10.3390/ijms23031135

Rahmani, M., Pham, T., Crossman, D. J., Tran, K., Taberner, A. J., & Han, J.-C. (2024). Sex differences in cardiac energetics in the rat ventricular muscle. *Scientific Reports*, *14*(1), 31242. https://doi.org/10.1038/s41598-024-82604-3

Ravizzoni Dartora, D., Flahault, A., Pontes, C. N. R., He, Y., Deprez, A., Cloutier, A., Cagnone, G., Gaub, P., Altit, G., Bigras, J. L., Joyal, J. S., Mai Luu, T., Burelle, Y., & Nuyt, A. M. (2022). Cardiac Left Ventricle Mitochondrial Dysfunction After Neonatal Exposure to Hyperoxia: Relevance for Cardiomyopathy After Preterm Birth. *Hypertension*, *79*(3), 575-587. https://doi.org/10.1161/hypertensionaha.121.17979

Reiser, P. J., Portman, M. A., Ning, X.-H., & Moravec, C. S. (2001). Human cardiac myosin heavy chain isoforms in fetal and failing adult atria and ventricles. *American Journal of Physiology-Heart and Circulatory Physiology*, *280*(4), H1814-H1820. https://doi.org/10.1152/ajpheart.2001.280.4.H1814

Saad, N. S., Mashali, M. A., Repas, S. J., & Janssen, P. M. L. (2023). Altering Calcium Sensitivity in Heart Failure: A Crossroads of Disease Etiology and Therapeutic Innovation. *Int J Mol Sci*, *24*(24). https://doi.org/10.3390/ijms242417577

Sharifi Kia, D., Kim, K., & Simon, M. A. (2021). Current Understanding of the Right Ventricle Structure and Function in Pulmonary Arterial Hypertension [Review]. *Frontiers in Physiology*, *Volume 12 - 2021*. https://doi.org/10.3389/fphys.2021.641310

Sixtus, R. P., Dyson, R. M., & Gray, C. L. (2024). Impact of prematurity on lifelong cardiovascular health: structural and functional considerations. *npj Cardiovascular Health*, *1*(1), 2. https://doi.org/10.1038/s44325-024-00002-0

Tedford, R. J., Hassoun, P. M., Mathai, S. C., Girgis, R. E., Russell, S. D., Thiemann, D. R., Cingolani, O. H., Mudd, J. O., Borlaug, B. A., Redfield, M. M., Lederer, D. J., & Kass, D. A. (2012). Pulmonary capillary wedge pressure augments right ventricular pulsatile loading. *Circulation*, *125*(2), 289-297. https://doi.org/10.1161/circulationaha.111.051540

Tewari, S. G., Bugenhagen, S. M., Palmer, B. M., & Beard, D. A. (2016). Dynamics of cross-bridge cycling, ATP hydrolysis, force generation, and deformation in cardiac muscle. *J Mol Cell Cardiol*, *96*, 11-25. https://doi.org/10.1016/j.yjmcc.2015.02.006

Tran, K., Han, J.-C., Crampin, E. J., Taberner, A. J., & Loiselle, D. S. (2017). Experimental and modelling evidence of shortening heat in cardiac muscle. *The Journal of Physiology*, *595*(19), 6313-6326. https://doi.org/https://doi.org/10.1113/JP274680

Velten, M., Heyob, K. M., Rogers, L. K., & Welty, S. E. (2010). Deficits in lung alveolarization and function after systemic maternal inflammation and neonatal hyperoxia exposure. *Journal of Applied Physiology*, *108*(5), 1347-1356. https://doi.org/10.1152/japplphysiol.01392.2009

Vinnakota, K. C., & Bassingthwaighte, J. B. (2004). Myocardial density and composition: a basis for calculating intracellular metabolite concentrations. *American Journal of Physiology-Heart and Circulatory Physiology*, *286*(5), H1742-H1749. https://doi.org/10.1152/ajpheart.00478.2003

Wearing, O. H., Chesler, N. C., Colebank, M. J., Hacker, T. A., Lorenz, J. N., Simpson, J. A., & West, C. R. (2025). Guidelines for assessing ventricular pressure-volume relationships in rodents. *American Journal of Physiology-Heart and Circulatory Physiology*, *328*(1), H120-H140. https://doi.org/10.1152/ajpheart.00434.2024